REPORT NO. DOT-TSC-NASA-73-1

DEVELOPMENT OF A PHOTOEMISSION SURFACE FOR 1.06 MICRON WAVELENGTH

L. W. James, R. L. Moon, G. A. Antypas,
J. Edgecumbe, and R. L. Bell

Varian Associates
611 Hansen Way
Palo Alto, CA 94303

February 1973

FINAL REPORT

Document is available to the
public through the National
Technical Information Service,
Springfield, Virginia 22151.

Prepared for:

DEPARTMENT OF TRANSPORTATION
TRANSPORTATION SYSTEMS CENTER
Kendall Square
Cambridge, MA 02142

TECHNICAL REPORT STANDARD TITLE PAGE

1. Report No. DOT-TSC-NASA-73-1	2. Government Accession No.	3. Recipient's Catalog No.
4. Title and Subtitle DEVELOPMENT OF A PHOTOEMISSION SURFACE FOR 1.06 MICRON WAVELENGTH		5. Report Date February 1973
		6. Performing Organization Code
7. Author(s) L.W. James et al		8. Performing Organization Report No. DOT-TSC-NASA-73-1
9. Performing Organization Name and Address Varian Associates 611 Hansen Way Palo Alto, CA 94303		10. Work Unit No. NA03/R1019
		11. Contract or Grant No. DOT-TSC-95
12. Sponsoring Agency Name and Address U.S. Department of Transportation Transportation Systems Center Kendall Square, Cambridge, MA 02142		13. Type of Report and Period Covered Final Report March 1971 - June 1972
		14. Sponsoring Agency Code

15. Supplementary Notes

16. Abstract

Development of a negative affirmity photoemitter with 10% quantum efficiency at the Nd^{3+} laser wavelengths near 1.06 microns.

Observed quantum yield of 7.55% (electrons per incident photon - 11% per absorbed photon) at 1.06 microns, from an InGaAsP quaternary cathode activated with (Cs,O) and cooled to $-90^{o}C$.

17. Key Words	18. Distribution Statement Document is available to the public through the National Technical Information Service, Springfield, Virginia 22151.		
19. Security Classif. (of this report) Unclassified	20. Security Classif. (of this page) Unclassified	21. No. of Pages	22. Price

Form DOT F 1700.7 (8-69)

TABLE OF CONTENTS

LIST OF ILLUSTRATIONS

LIST OF ILLUSTRATIONS (Contd.)

PREFACE

This is the final report on a program aimed at development of a negative-affinity photoemitter with 10% quantum efficiency at the Nd^{3+} laser wavelengths near 1.06 microns. This was essentially achieved with an observed quantum yield of 7.55% (electrons per incident photon--11% per absorbed photon) at 1.06 microns, from an InGaAsP quaternary cathode activated with (Cs,O) and cooled to -90°C.

The report describes the development approaches leading to this result--investigation of different crystal faces of a number of different ternary and quaternary compounds including InAsP, InGaAs, GaAsSb, InSbP, InAlAs, GaAlSb, GaAlAsSb, and InGaAsP, of different activator materials and configurations, and different preparation procedures and doping schemes.

Several photosurfaces from the InAsP/InGaAsP family gave room-temperature yields in the 3-6% region at 1.06 microns. A beginning was made in the crucial area of stabilizing this type of performance in sealed-off tubes. Increasing success has been observed (the highest InAsP yield, 5.5%, was measured in a sealed-off diode) but deeper understanding of this area, and further development are urgently needed.

THE MODEL

The model which we use to characterize III-V semiconductor photocathodes is the heterojunction model shown in Fig. 1. Cs_2O is an n-type semiconductor with a 2.0 eV bandgap, a 0.4 to 0.5 eV electron affinity, and a large density of deep (0.2 eV) donor levels caused by excess cesium (Ref. 1). The Cs_2O forms a heterojunction with the III-V semiconductor with band bending in both materials. The band bending in the Cs_2O accounts for the observed (Ref. 2) parabolic decrease in work function with increasing Cs_2O thickness (assuming that the Cs_2O electron affinity remains approximately constant). The Cs_2O conduction band at the interface gives an interfacial barrier. The amount of band bending in both the III-V semiconductor and the Cs_2O is a function of the surface states at the interface. These surface states will vary from material to material, and even with different crystal orientation or methods of surface preparation for the same material. Thus we can expect variations in the heterojunction barrier height.

Let us examine the type of yield curves which can be expected for photocathodes for which this model is applicable. Figure 2 shows, on the left, the heterojunction model band diagram and, on the right, the yield curves for three cases.

At the top is the model for a III-V semiconductor with a bandgap much larger than the heterojunction barrier height, such as GaAs. Electrons from the GaAs conduction band escape with a high probability over all barriers, resulting in the high yield experimental curve shown on the right.

Figure 3 shows electron energy distribution curves measured from a Cs_2O-activated InP sample. Notice that, while most of the emission is contained in the two peaks which come from electrons thermalized in the conduction band minima, for photon energies above the bandgap an increasingly significant portion is emitted as hot electrons between the two minima.

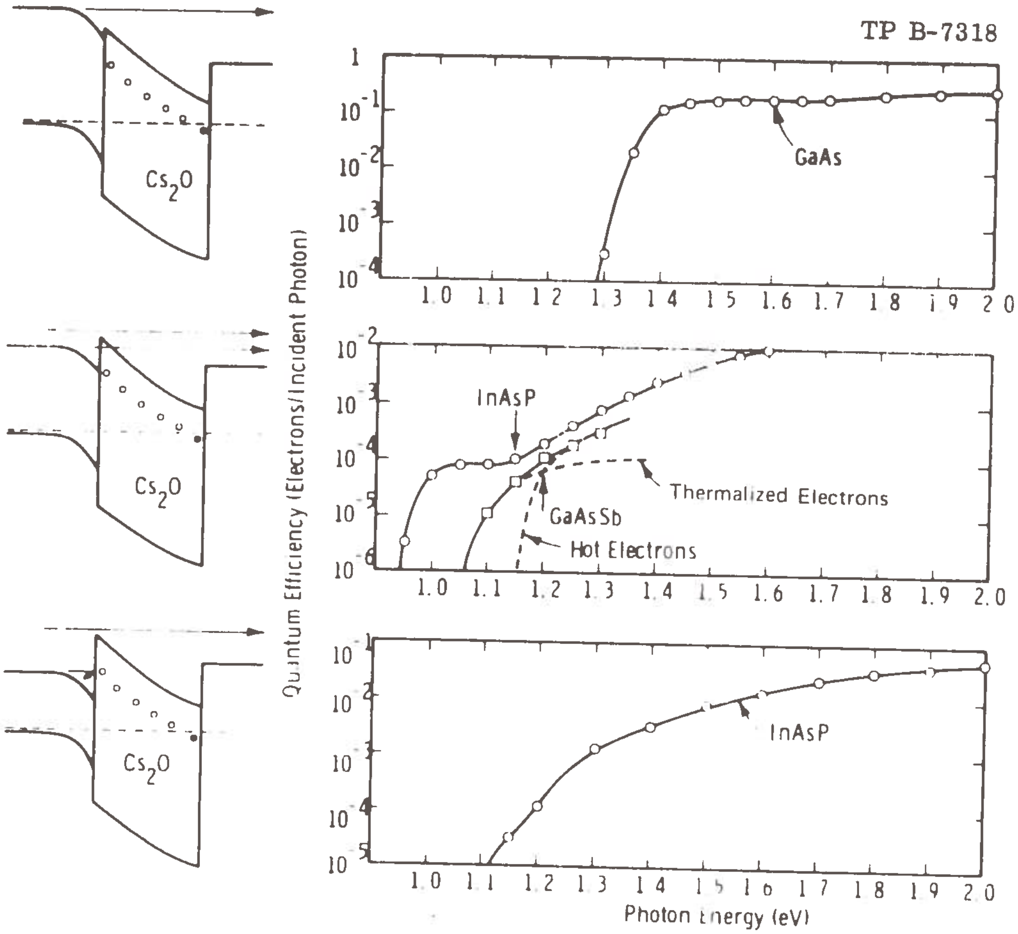

Figure 2. Band Diagrams (on the left) and Yield Curves (on the right) Demonstrating the Emission Mechanisms for Semiconductor Materials with Bandgaps Larger than the Heterojunction Barrier Height (top), with Bandgaps Slightly Less than the Heterojunction Barrier (middle), and with Bandgaps much Smaller than the Heterojunction Barrier Height (bottom).

In the middle of Fig. 2 is shown the model for a semiconductor with a bandgap slightly less than the heterojunction barrier height. Electron emission comes from two processes: thermalized electrons in the lowest conduction band with a low escape probability, and hot electron emission over the barrier with a high excape probability. This is clearly seen in the experimental InAsP yield curve where for photon energies below 1.15 eV the yield comes from electrons thermalized in the conduction band with total escape probability of about 10^{-4}. For photon energies above 1.15 eV, hot electrons are emitted over the barrier with a much higher escape probability, and the yield rises. A yield curve with a very similar shape was obtained by Williams (Ref. 3) on InGaAs, showing clear evidence of a heterojunction barrier on that material.

For a III-V semiconductor with a bandgap closer to the heterojunction barrier and/or with a poorer diffusion length as demonstrated by the experimental GaAsSb curve, it can be impossible to see any structure on the yield curve at the heterojunction barrier energy in spite of the fact that there are two components to the yield. If one misapplies the diffusion model (Ref. 4) (which has as a basic assumption the complete thermalization in conduction band minima) to try to fit the yield curve from a cathode of this type, he obtains a diffusion length which is much too short and, perhaps more importantly, an escape probability which is much too high.

Shown at the bottom of Fig. 2 is the case for a small bandgap semiconductor such as the 0.6 eV bandgap InAsP sample shown. Electrons thermalized in the lowest conduction band see such a thick barrier that their escape probability is negligible. For photon energies higher than the heterojunction barrier, hot electron emission is responsible for the yield, and the barrier height determines the yield threshold. (There will always be a small yield at lower photon energies due to photoemission from the Cs_2O layer.)

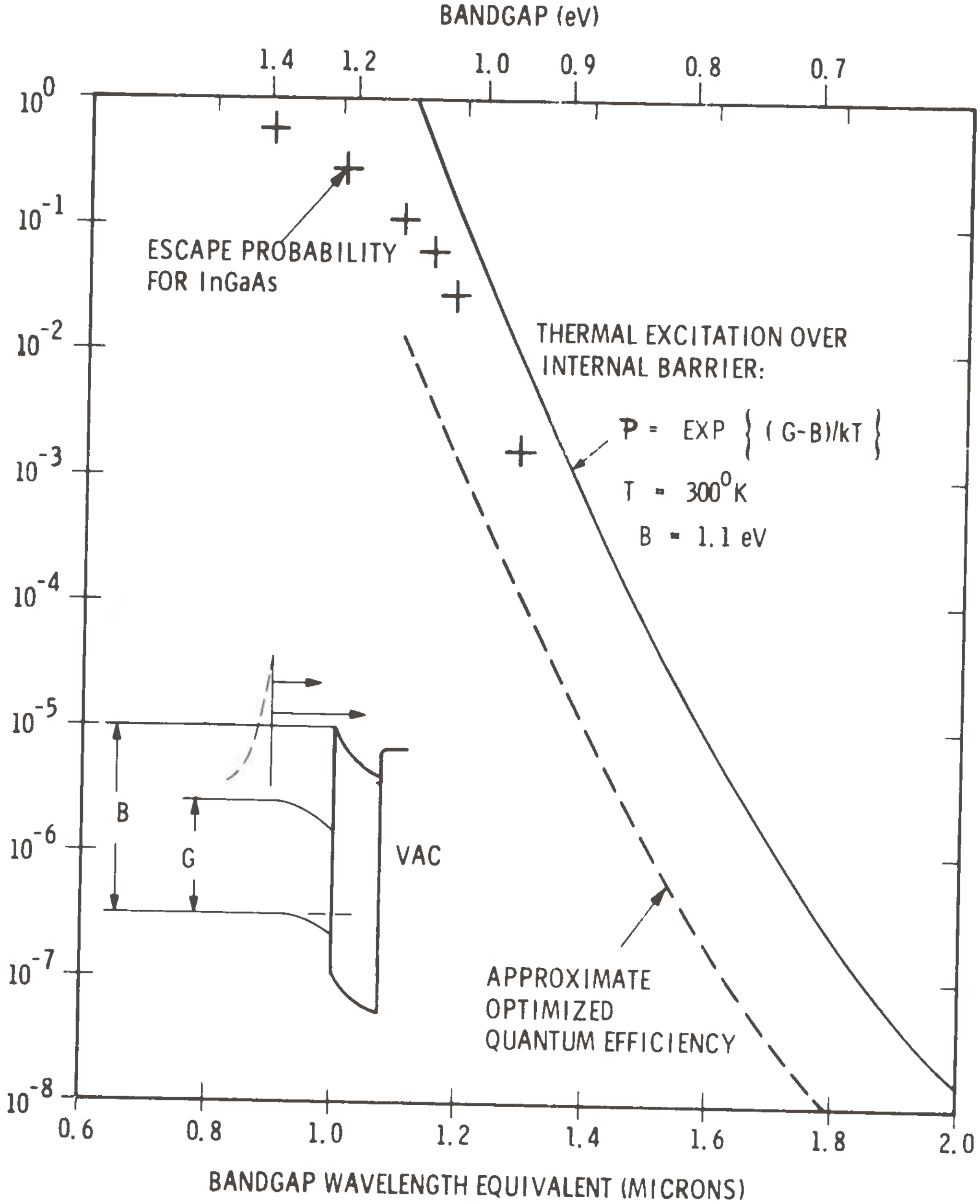

Figure 4. Comparison of the escape probability for InGaAs experimental data from Ref. 6 with the escape probability predictions of a simplified model, shown as the insert, where the hot electron tail of the thermalized electron distribution passes unopposed over the interfacial barrier while the lower energy electrons are reflected.

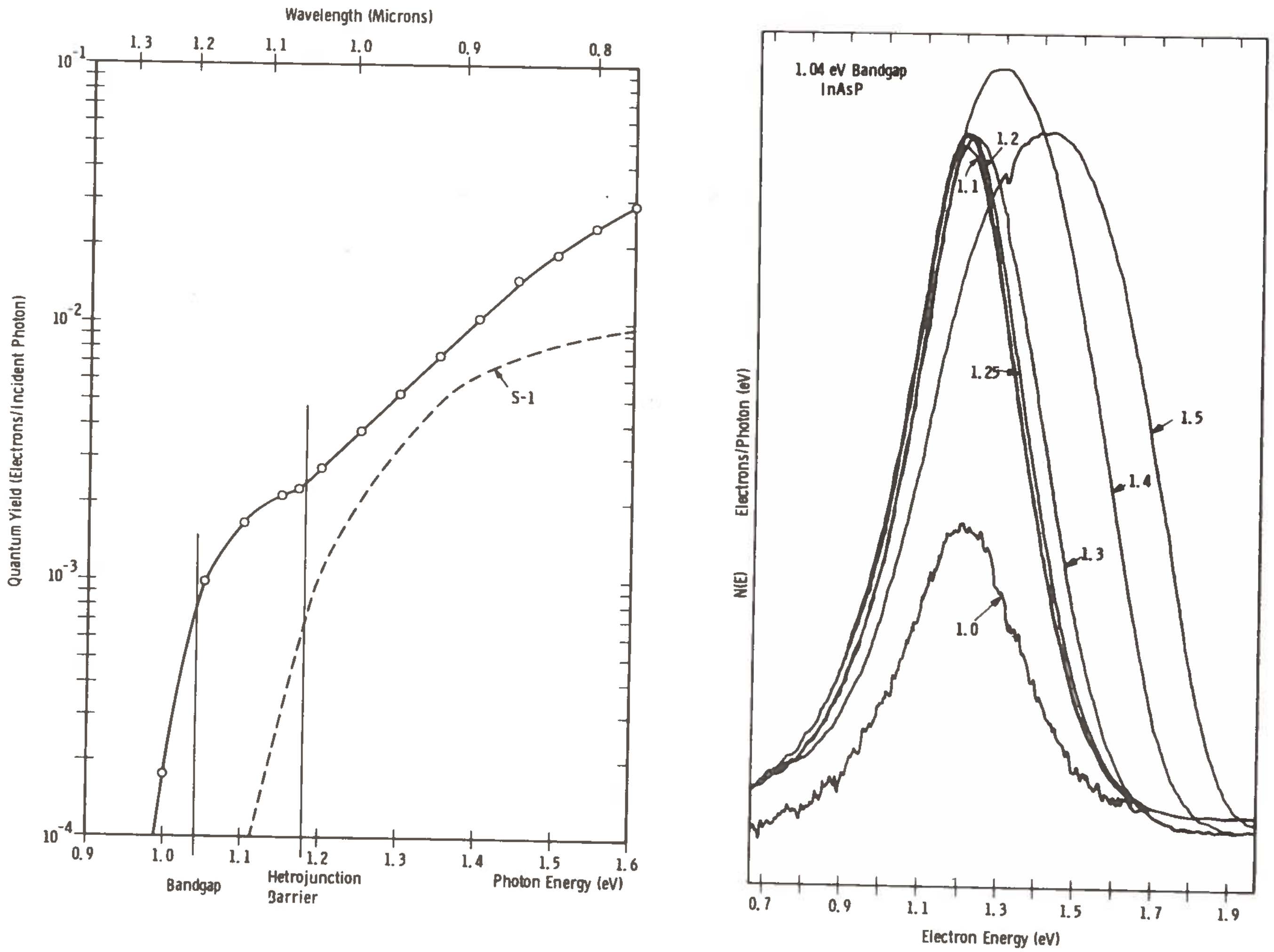

Figure 5. Quantum Yield and Photoelectron Energy Distribution Curves from a $10^{19}/cm^3$ Zn-Doped 1.04 eV Bandgap InAsP Sample. For photon energies below the barrier height, the energy distribution shape is identical within the resolution of the analyzer. For higher photon energies, hot electrons start to appear at energies above the barrier height.

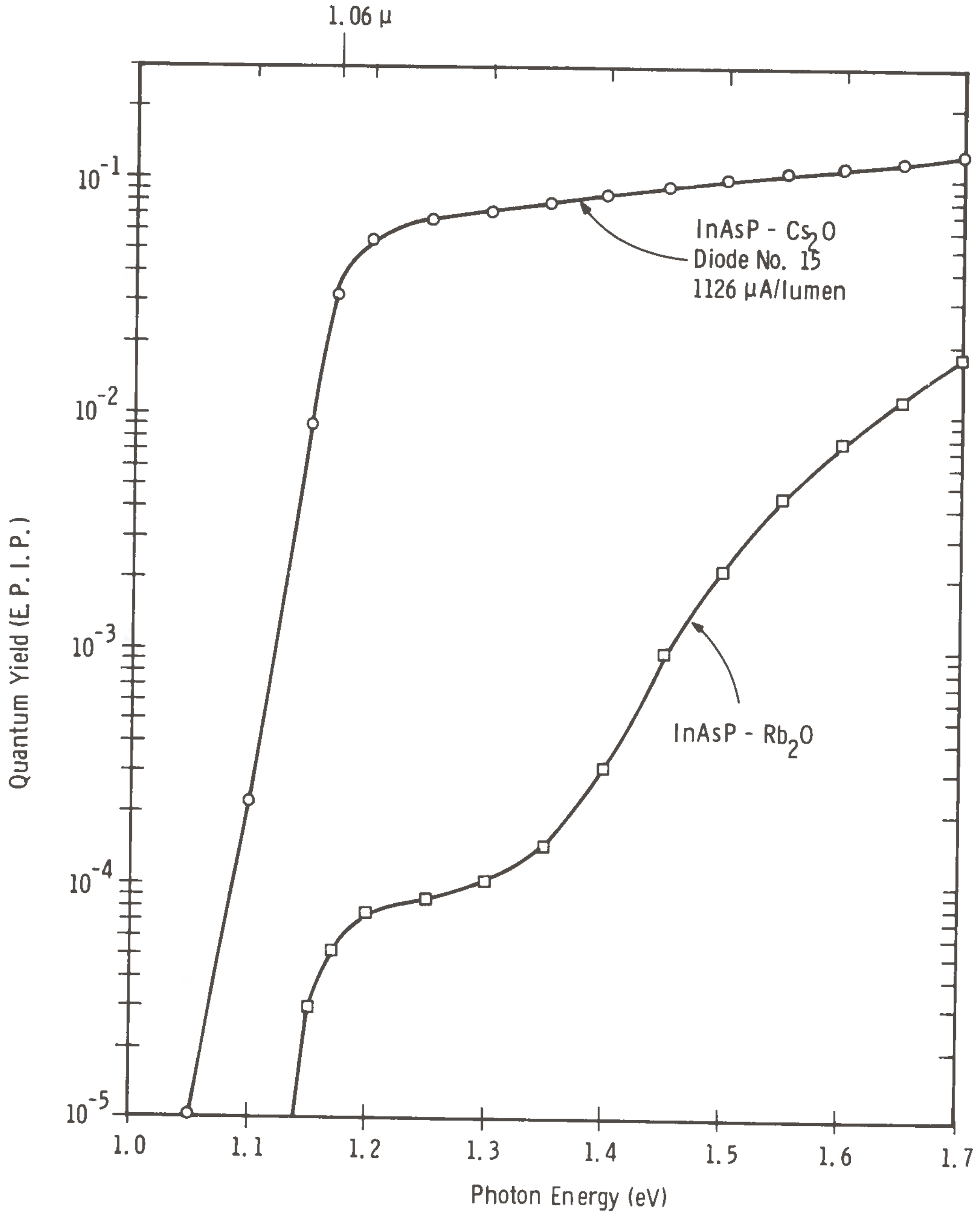

Figure 6. Comparison of the Yield Curves for the Cases of G > B (InAsP-Cs_2O) and G < B (InAsP-Rb_2O). The (InAsP-Cs_2O) sample was measured in a sealed-off diode tube. The (InAsP-Rb_2O) sample was an identical liquid epitaxial sample, with Rb substituted for Cs in the activation process.

T_{ABS} accounts for those electrons which are absorbed through scattering, trapping, and recombination while passing through the Cs_2O layer. T_{BV} is the transmission over the work function barrier into the vacuum. As the Cs_2O thickness is increased, T_{ABS} decreases since the electrons have a greater chance of being absorbed when passing through a thicker layer. T_{BV}, on the other hand, increases with increasing Cs_2O thickness because the decreasing work function* allows increased transmission over the barrier. For any given III-V semiconductor sample, there is an optimum Cs_2O thickness which maximizes the product $T_{ABS} \cdot T_{BV}$. In comparing semiconductors, a larger energy difference between the bandgap and the heterojunction barrier means that the product $T_{ABS} \cdot T_{BV}$ peaks with a thinner Cs_2O layer, and the peak has a higher value.

In order to get a firmer grasp on the heterojunction model, it may be helpful to discuss the various tradeoffs involved in optimizing for a given photon energy in terms of the specific example of the state-of-the-art at the beginning of this contract for 1.06-micron optimized Zn-doped InAsP with a quantum efficiency of 2.2% per incident photon. Fitting the data for this cathode to the heterojunction model gives the following values for the terms in the yield equation:

$$(1-R) = 0.71$$

$$(1+1/\alpha L)^{-1} = 0.27$$

$$T_{BB} \cdot T_{BS} = 0.67$$

$$T_{ABS} = 0.24$$

$$T_{BV} = 0.71$$

Figure 7 shows how T_{ABS} and T_{BV} vary with Cs_2O thickness, resulting in a maximum product at the values shown. T_{BV} is zero for a Cs_2O thickness less than 1.7 Langmuirs (micro-torr seconds) of oxygen

---

* The Cs_2O electron affinity stays approximately constant through the Cs_2O band-bending region.

exposure because the work function is higher than the bottom of the conduction band. T_{ABS} is obtained simply from the characteristic electron absorption length in Cs_2O, and hence takes the form of a simple exponential decay with thickness. The $T_{BV} \cdot T_{ABS}$ product is discussed more fully in Ref. 2. $T_{BB} \cdot T_{BS}$ can, of course be obtained from the measured value of P, once $T_{BV} \cdot T_{ABS}$ is known. The number for $(1+1/\alpha L)^{-1}$ looks particularly small for an optimized cathode. It is small in spite of a reasonable diffusion length (approximately 2 microns) because the incident light (at 1.17 eV) is less than the InAsP bandgap (but still in the exciton absorption range) resulting in a very small α. However, if the bandgap is lowered to increase α, $T_{BB} \cdot T_{BS}$ drops rapidly due to the heterojunction barrier. For example, with a 1.15 eV bandgap:

$(1-R) = 0.71$

$(1+1/\alpha L)^{-1} = 0.50$

$T_{BB} \cdot T_{BS} = 0.29$

$T_{ABS} = 0.21$

$T_{BV} = 0.70$

for a quantum efficiency of only 1.5% per incident photon.

From the model and these examples, it is clear that the largest improvement in 1.06-micron quantum efficiency would be obtained by lowering the heterojunction barrier. With a lower barrier, $T_{BB} \cdot T_{BS}$ would be higher, the required Cs_2O thickness would be reduced raising T_{ABS}, and a lower bandgap material could be used, raising $(1+1/\alpha L)^{-1}$. The position of the heterojunction barrier is determined by surface states at the III-V-Cs_2O interface. Various possibilities suggest themselves as ways of affecting these surface states and lowering this barrier:

A. Use of different crystalline faces of the III-V material.

B. Use of other III-V materials.

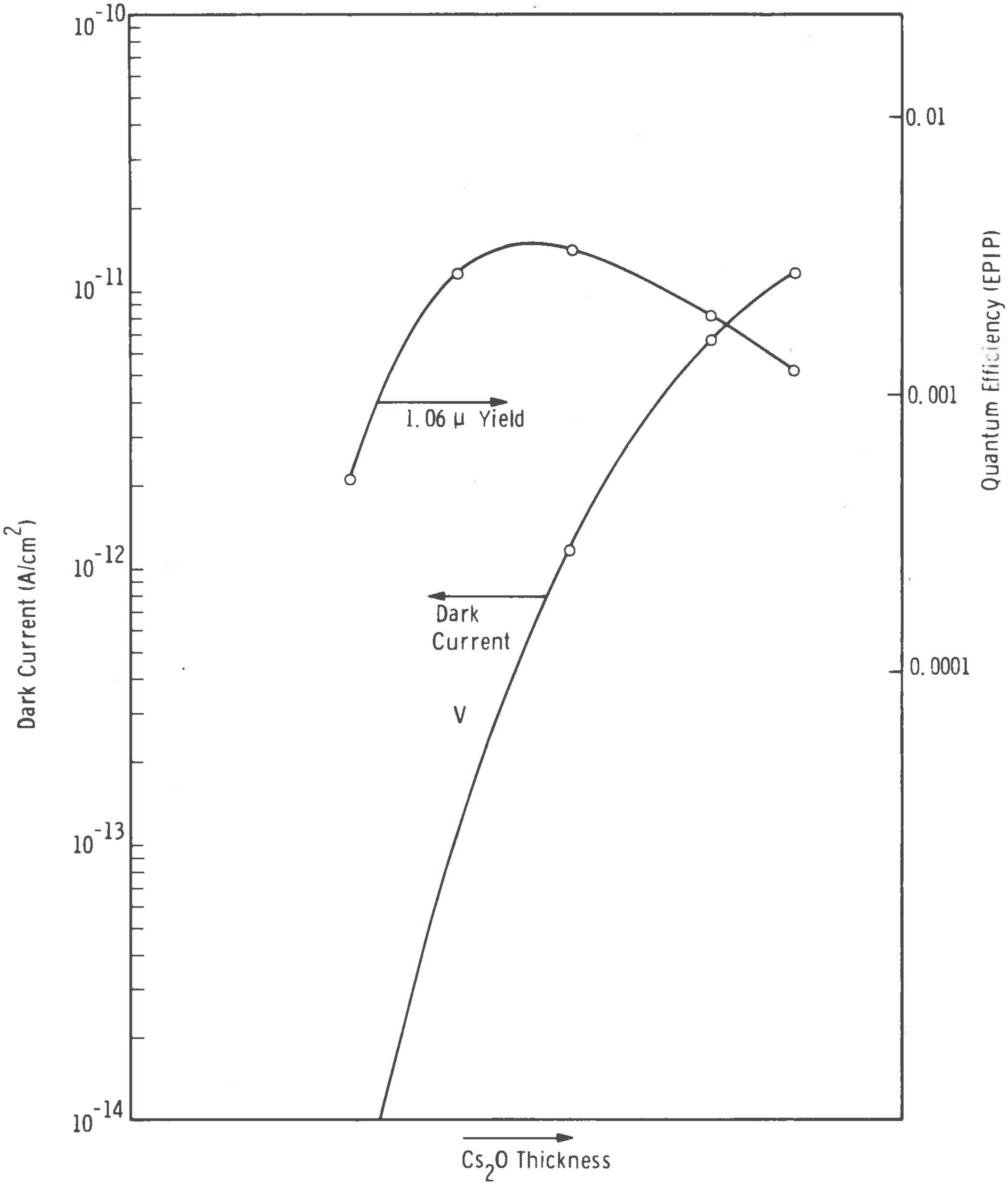

TP B-7247

Figure 8. Dark Current and 1.06 Micron Yield as a Function of Cs$_2$O Thickness for an InAsP Photocathode. The "V" indicates the limiting sensitivity of the dark current measurement.

photocathode quantum yield, particularly near threshold. Thus the optimum doping is a compromise between diffusion length and escape probability.

If the amount of the band bending V_{BB} could be reduced, the doping concentration N_A could be similarly reduced, giving a longer diffusion length without affecting W or the escape probability. We have shown earlier that for both InAsP (Ref. 10) and GaAs (Ref. 1), a Cs_2O activation layer produces a smaller amount of band bending than a Cs monolayer alone. This, combined with the fact that more energy loss is allowable in the band-bending region due to the lower Cs_2O work function, makes the optimum doping density for a Cs_2O-activated GaAs photocathode lower than that for a Cs-activated GaAs photocathode. However, reducing the band bending even more should result in a further improvement.

The original work on GaAs-Cs_2O photocathodes (Refs. 16 and 17) was done on cleaved surfaces, which were always {110} planes. Most recent work has been on as-grown or polished epitaxial layers which are cleaned by heating in ultrahigh vacuum to near the congruent evaporation point. Our LEED studies show that epitaxial layers which are not originally {110} surfaces will facet to give {110} surfaces during the normal heat cleaning cycle. Thus the majority of the results appearing in the literature for GaAs photocathodes are probably relevant for {110} surfaces.

In order to compare the GaAs-Cs_2O band-bending parameters for different crystalline faces, it was necessary to produce as clean a surface as practical outside the vacuum system, to place the sample into the vacuum system through a vacuum interlock, and to carry out prolonged heat treatments just below the faceting temperatures. Figures 9 through 12 show the results of quantum yield measurements made on these clean unfaceted surfaces of n-type GaAs samples of {110}, {100}, {111A}, and {111B} orientation when activated with several molecular layers of Cs_2O.

At the right of each figure is a threshold plot, plotting $(\text{yield})^{1/2}$ vs photon energy to determine the threshold photon energy for each photoemission process. On the left at the top is the band diagram deduced from the threshold plot for n-type material. At the bottom left is the corresponding band diagram for p-type material, assuming that the surface Fermi level is not changed by changing the bulk doping.

Looking at Fig. 9, we can see that there are three photoemission processes, each with a different threshold. The process with the lowest threshold is photoemission from donor levels in the Cs_2O, with a threshold at 0.98 eV determined by the work function. The next process is photoemission from surface states and/or the GaAs conduction band, with a threshold limited by the heterojunction barrier at 1.32 eV above the Fermi level. The most efficient photoemission process is photoemission from the GaAs valence band in the band-bending region, with a threshold of 1.55 eV given by the surface valence band to heterojunction barrier energy spacing. It is clear that this threshold is not determined by the surface valence band to vacuum level spacing because this threshold remains constant at 1.55 eV (along with the heterojunction barrier threshold which remains constant at 1.32 eV) as the Cs_2O is made thicker causing the threshold corresponding to the work function to decrease. It should be noted that this Cs_2O layer is many times thicker than that required for optimum photoyield from a p-type GaAs sample (Ref. 1). Knowing these thresholds, as shown on the right side of the n-type band diagram, along with the GaAs bandgap of 1.42 eV, a little arithmetic gives us the Fermi level position at the GaAs-Cs_2O interface.

Figure 10 shows the results for a {100} surface. Note that with this particular Cs_2O thickness there is actually a dip in the quantum yield curve. For photon energies less than the barrier height, all electrons excited from filled Cs_2O donor states are repelled by the heterojunction barrier and accelerated by the band-bending field toward the emitting surface. For photon energies larger than the barrier height, those electrons generated in the Cs_2O with velocities in the direction of the barrier will go over the barrier and be lost in the GaAs. Thus the yield decreases for photon energies above the barrier height. Note that the peak in the yield (indicated by the vertical dashed line) and the extrapolation to zero of the threshold yield plot both give the same values for the heterojunction barrier height. Except for the work function, which is dependent on Cs_2O thickness, the thresholds for this sample, and therefore the GaAs-Cs_2O heterojunction parameters, are the same within experimental accuracy as those of the {110} sample.

Figure 11 shows the results measured for a {111A} sample. On this sample the Cs_2O is so thick (0.91 eV work function) that photoyield from the Cs_2O donor levels is more efficient (i.e., has a higher quantum efficiency) than photoyield from surface states or the GaAs conduction band. Thus the emission from surface states or the conduction band is not seen as a separate threshold on the threshold plot. The heterojunction barrier height can still be obtained, however, from the position of the peak just before the dip in the yield curve, as on the {100} sample. Note that while the heterojunction barrier height of 1.32 eV is the same (within experimental accuracy) for the {110} and {100} faces, the amount of band bending in the GaAs differs considerably. Hoene (Ref. 18) gives optical absorption data on Cs_2O. Using his value of 2.2 eV for the Cs_2O bandgap, the Cs_2O valence band is found to be aligned with the GaAs valence band (Ref. 1) on this face.

In order to confirm the LEED results, a {111A} n-type sample was heated to the temperature where faceting occurred. Yield data were then taken after Cs_2O activation. The threshold plot gave results practically identical to those for a {110} surface, and considerably different from those of an unfaceted {111A} surface.

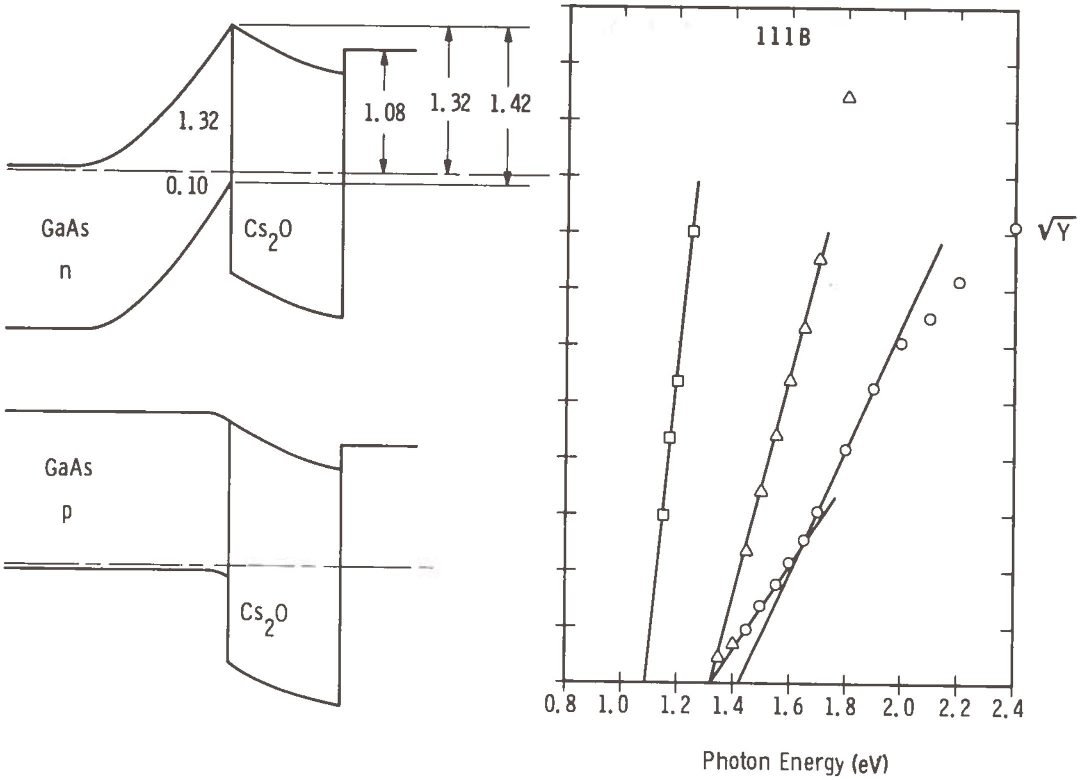

Figure 12. Threshold Yield Plot for a Cs$_2$O-Activated (111B) N-Type GaAs Sample. The △ points are multiplied by 2.5 before plotting, and the □ points are multiplied by 100 before plotting. The measured quantum efficiency at 2.0 eV was 5.6 x 10^{-3} electrons per absorbed photon.

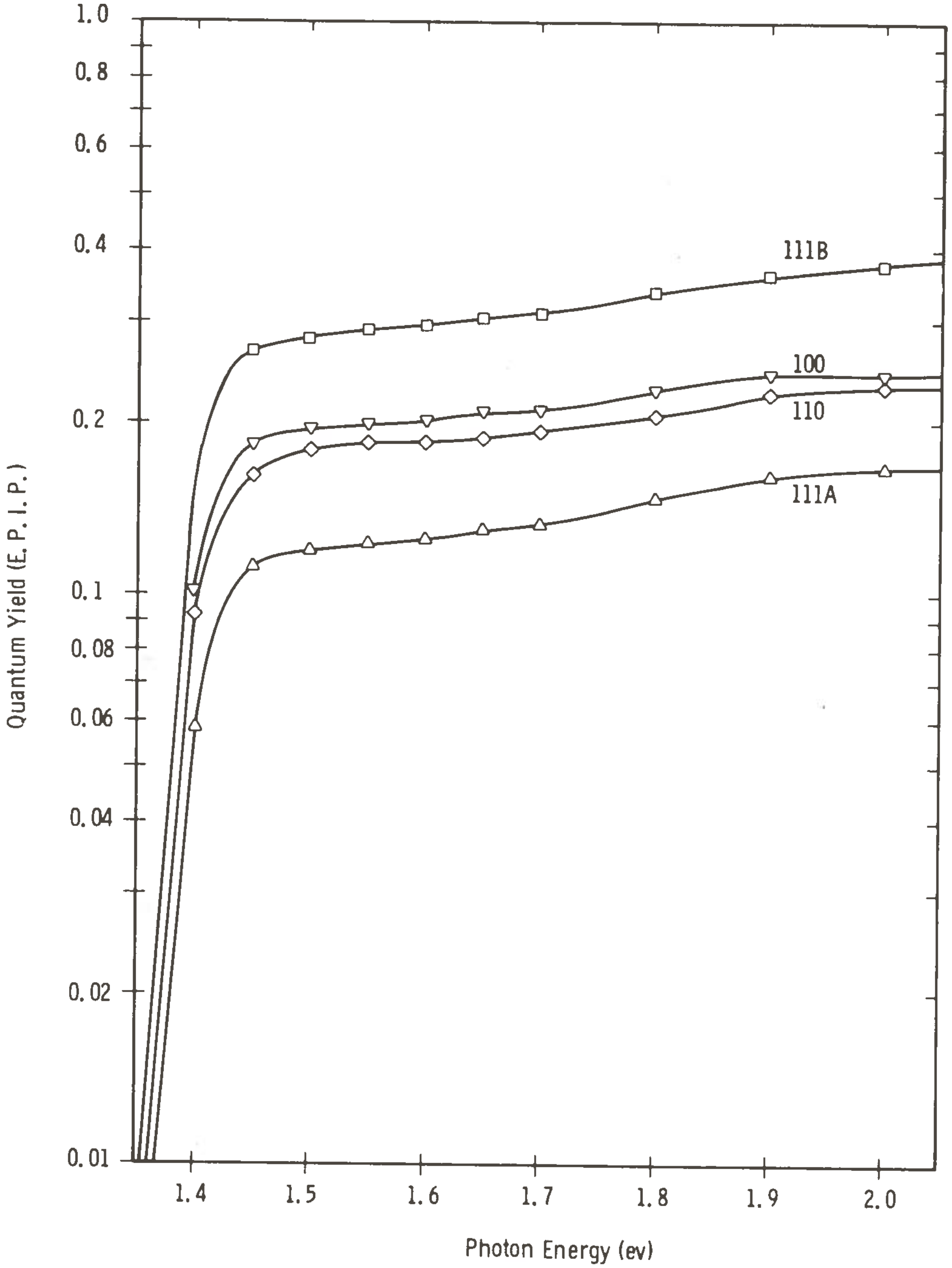

Figure 13. Photoelectric Quantum Efficiencies in Electrons Per Incident Photon for 5 x $10^{18}/cm^3$ Zn-Doped Liquid Epitaxial GaAs Samples. The four curves are for (111A), (110), (100), and (111B) surfaces cleaned in the same manner as the n-type samples of Figures 9 through 12 to avoid faceting, and activated to the peak luminous sensitivity with alternate exposures of cesium and oxygen.

TABLE I

Experimental Parameters of Low Index Faces of 5 x 10^{18} Zn-Doped GaAs

(Diffusion Length = 6 Microns)

Crystal Face	P-Type Band Bending	Band Bending Width	Conduction Band Step	Escape Probability	Luminous Sensitivity
{111A}(Ga)	0.86 eV	155 Å	0.76 eV	.212	810 μA/lm
{100}	0.28 eV	88 Å	0.18 eV	.317	1225 μA/lm
{110}	0.23 eV	80 Å	0.13 eV	.307	1125 μA/lm
{111B}(As)	0.10 eV	51 Å	0 eV	.489	1837 μA/lm

The heterojunction barrier height is measured using photoemission from an n-type sample as discussed in the previous section. GaAsSb and InSbP were shown to be less desirable materials than InAsP for 1.06-micron photocathodes because of their larger heterojunction barrier heights. The barrier height as a function of bandgap for these materials is shown at the top of Fig. 15. The correlation between escape probability and barrier height is dramatically demonstrated by comparing the measured escape probability for these materials, shown in Fig. 16, with Fig. 15. Thus InSbP and GaAsSb are clearly less suitable than InAsP for 1.06-micron photocathodes because of their higher heterojunction barriers.

InGaAs and InAsP of the proper composition range for 1.06-micron photoemission have practically the same heterojunction barrier heights. InGaAs has only a slightly lower escape probability. The major difference between these two materials is in the obtainable diffusion lengths. Good InAsP liquid epitaxial material has an electron diffusion length of 4-5 microns, while the best liquid phase or vapor phase InGaAs material has a diffusion length of only 1 micron or less. Figure 17 shows a comparison between the yield curves of two InGaAs photocathodes and an InAsP photocathode. Notice the more rounded corner near threshold of the InGaAs samples which is characteristic of a shorter diffusion length. Barring any future materials development which results in InGaAs with a longer diffusion length, this material may also be removed from consideration.

GaSbP has not been tried because to obtain the proper bandgap the alloy would have to be grown near the middle of the composition range. This mid-range composition is difficult to grow in any alloy system, and would be especially difficult in this system because of the large difference in lattice constants between the two binary constituents. In addition to the materials growth problems, all Sb-bearing materials tested have a high heterojunction barrier, making it very likely that this material would have a high barrier also if it could be grown.

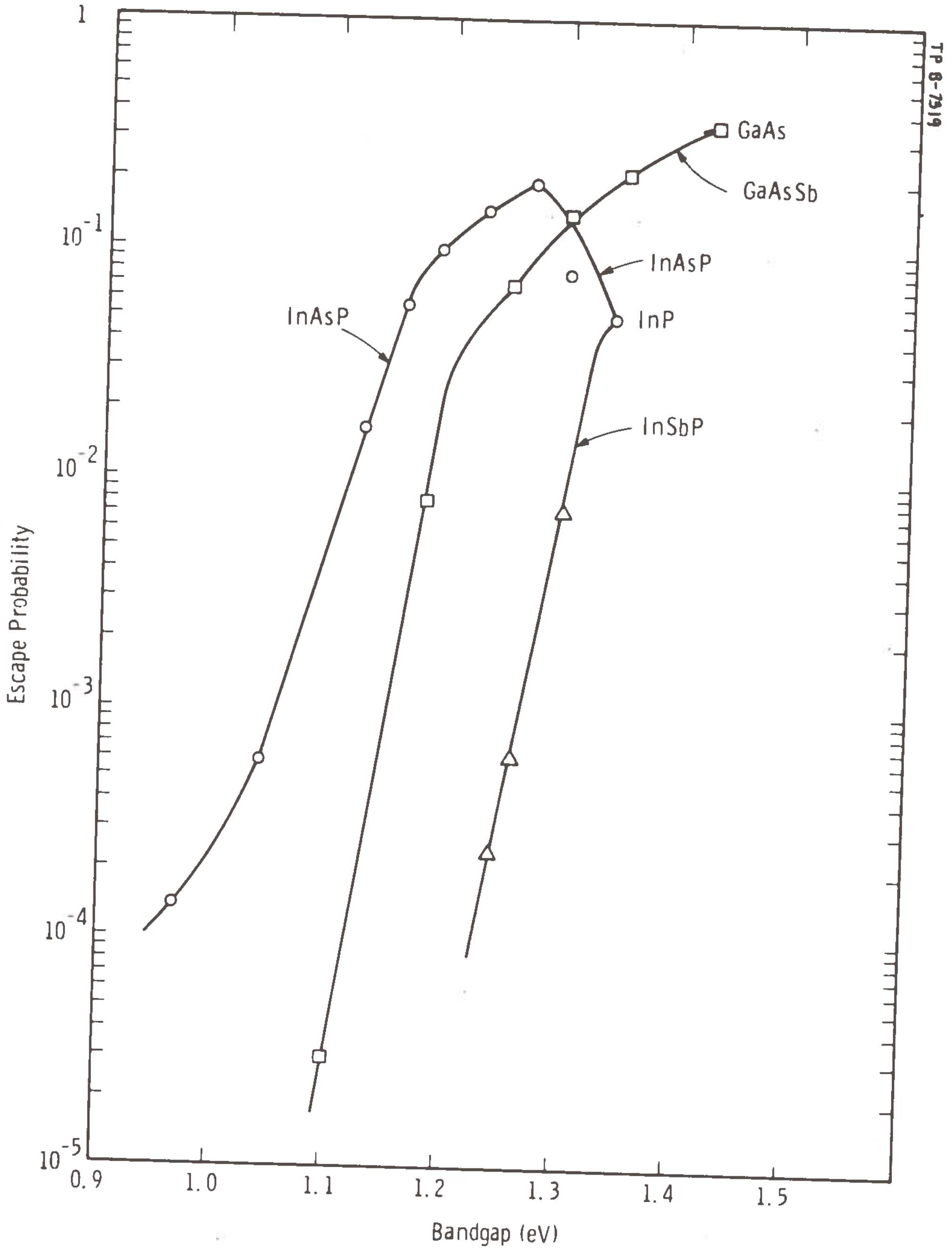

Figure 16. Photocathode Escape Probability vs Bandgap as Measured for p^+ InAsP, InSbP, and GaAsSb Ternary Epitaxial Layers.

The three remaining ternary compounds contain Al. GaAlSb has an indirect rather than a direct bandgap in the bandgap range of interest. This is undesirable for photoemission because indirect bandgap materials have a much lower optical absorption coefficient, α, near the bandgap than direct bandgap materials. This makes the quantum yield lower (see Eq. (3)). Both InAlSb and InAlAs would require compositions near the 0.50-0.50 point in order to have the correct bandgap. InAlSb of the proper composition would probably (from available band structure information) be very close to the crossover between direct and indirect bandgap. If it were on the indirect side of the crossover, the same comments made about GaAlSb would apply. Aluminum-bearing III-V compounds are difficult to work with because of the great affinity of Al for oxygen. Great pains must be taken to exclude all oxygen from the growth system. Successful measures to this end have been instituted, and good Al-bearing epitaxial layers have been grown. However, when the layers are exposed to air an aluminum-oxide layer is formed on the surface which is extremely difficult to remove.

Growth of GaAlAs is under better control than the other Al-bearing compounds, so experiments were done with GaAlAs to determine the effect of the Al concentration on the ease of removing surface oxygen. Auger spectroscopy shows that oxygen is removed from a GaAs surface by heating to approximately 550°C. Oxygen is removed from all Al-free III-V compounds at temperatures near this GaAs value. A sample of GaAlAs containing less than 5% AlAs was grown and tested for oxygen removal. This sample required a temperature approximately 100°C hotter than the GaAs sample to remove the surface oxygen. Samples with a higher Al concentration were decomposed by heating without removing the surface oxygen. Thus it appears impossible to remove the aluminum-oxide layer from the Al-bearing ternaries in the composition range of interest by our normal heat-cleaning procedures. The Al concentration builds up near the surface as it is bound to the oxygen present, and the

the regular solution model. If, however, the ternary is of the type III-III'-V, the γ_i^o's do not cancel and must be determined beforehand. Without extensive binary data Darken's model then requires two additional parameters which are difficult to estimate. On the other hand, when the data are available this method should provide a means of calculation, independent from the normal curve fitting procedures. Considering the above limitations, the regular solution appears the best for a first-order approximation when thermodynamic data are scanty. The necessary equations are adequately discussed elsewhere and are stated here without derivation.

In the ternary liquid the activity coefficient of each component is given by

$$RT\ln\gamma_i = \alpha_{ij}x_j^2 + \alpha_{ik}x_k^2 + (\alpha_{ij} + \alpha_{ik} - \alpha_{jk})x_j x_k \qquad (5)$$

where α_{ij} are the interaction parameters for the respective binaries (Ref. 23). The constants are determined by calculating the activity coefficients from vapor pressure data or by fitting the binary solubility data to Vieland's equation (Ref. 24) for a regular solution which is

$$\alpha = \frac{-RT}{2(0.5 - x)^2}\left[\ln 4x(1-x) + \frac{\Delta S^F}{R}\left(\frac{T^F}{T} - 1\right)\right], \qquad (6)$$

where x = atomic fraction in the liquid, ΔS^F = entropy of fusion, and T^F = temperature of fusion. Although Vieland's equation should yield a constant α, independent of temperature, all α's for III-V compounds have been shown to be linear functions of temperature (Ref. 25). The general form for the interaction parameter in a binary III-V system is then $\alpha = a-bT$ (quasi-regular solution).

For the psuedo-binary solid a regular solution approach is used also. Both the liquid and solid in equilibrium (solidus) are described by

$$RT\ln\gamma_{AC} = \alpha x_{BC}^2 \qquad (7a)$$

$$RT\ln\gamma_{BC} = \alpha x_{AC}^2 \qquad (7b)$$

$$\gamma_{BC}{}^{x} = \frac{4\gamma_B\gamma_C}{\gamma_B^{SL}\gamma_C^{SL}} x_B^L x_C^L \exp\left[\frac{\Delta S_{BC}^F}{RT}(T_{BC}^F - T)\right] \qquad (9b)$$

where γ_i^{SL}'s are the activity coefficients of the stoichiometric liquid and the rest of the variables have their usual meaning. The only assumption involved in the derivation of Eq. (9) is that the difference between the solid and liquid heat capacities is negligibly small. Combining the basic equations with the expressions for activity coefficients the solid composition in equilibrium with a melt can be obtained.

Most of the data for the $Ga_{1-x}Al_xSb$ system is readily available from the literature and the values used are summarized in Table II. $\alpha_{GaSb-AlSb}$ for the psuedobinary was obtained by fitting the liquidus and solidus data of Burdiyan and Borshchevskii (Ref. 29). Results of the calculation are shown in Fig. 18 where the liquidus and isoconcentration lines are shown for $x_{Sb} < 0.5$. In Fig. 19 the solid composition is shown as a function of Al concentration in the liquid. For a given x_{Al}, Fig. 19 shows that the AlSb concentration in the solid in equilibrium with a ternary liquid will increase with temperature. To obtain any appreciable concentration of Al in the solid the melt must contain more than 5% Al at all reasonable growth temperatures. Since aluminum forms a highly stable oxide, this indicates that LPE growth must be conducted in an oxygen-free system.

Parameters necessary for the calculation of the $In_{1-x}Al_xAs$ system are listed in Table III. In this case, the $\alpha_{III-III'}$ is no longer equal to zero, but is known to have a definite temperature dependence. From the heat and entropy of mixing data of Predel and Sandig (Ref. 30) the excess free energy can be calculated (Ref. 28) to be

$$\Delta G^x = \Delta H_M - T\Delta S^x = (6800 - 1.6\ T)x_{Al}x_{In} \quad . \qquad (10)$$

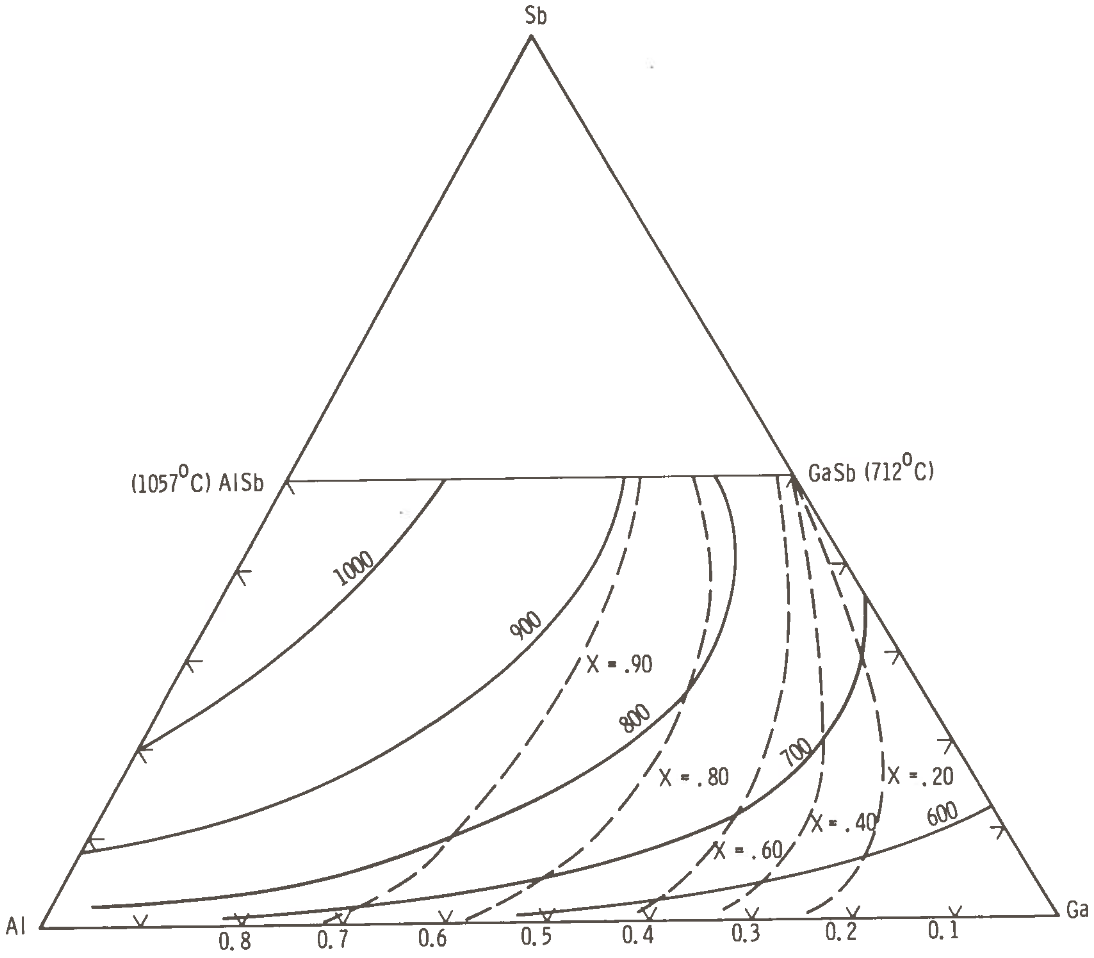

Figure 18. Calculated Liquidus and Isoconcentration Lines in the GaAlSb System for $x_{Sb} \le 0.5$

Table III

PARAMETERS USED FOR THE CALCULATION OF THE In-Al-As PHASE DIAGRAM

	InAs	AlAs
T_m	1215°K (Ref. 32)	2043°K (Ref. 31)
ΔS_m	14.52 eu (Ref. 32)	16 eu (est.) (Ref. 32)
α	$-9.160T + 4300$ cal/mole (Ref. 28)	$-9.16T + 9040$ cal/mole (Ref. 27)
ΔH_m	17,650 cal/mole (Ref. 32)	32,700 cal/mole (Ref. 32)

$\alpha_{In-Al} = 6800 - 1.6\ T$ cal/mole (Ref. 28)

$\alpha_{InAlAs} = 2000$ cal/mole

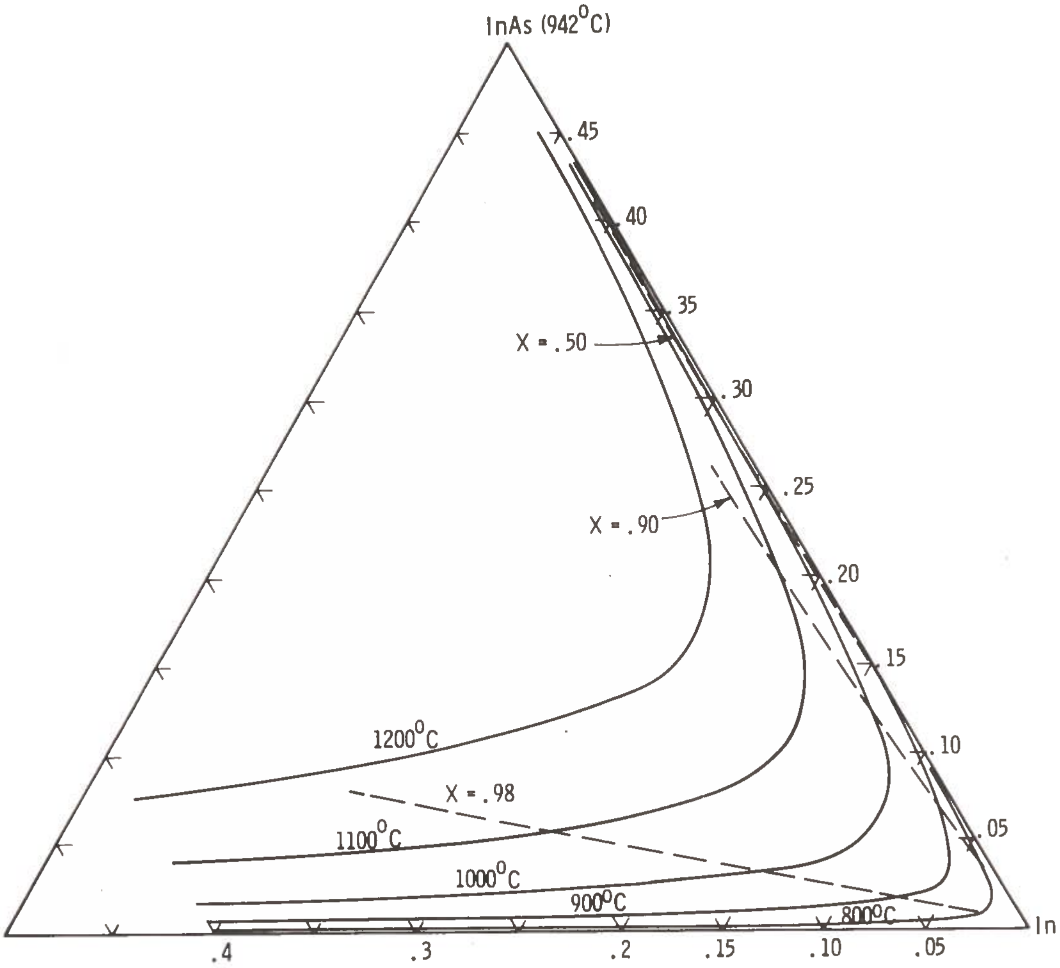

Figure 20. Calculated Liquidus and Isoconcentration Lines in the InAlAs System for $x_{As} \leq 0.5$, x = Concentration of AlAs in the Solid

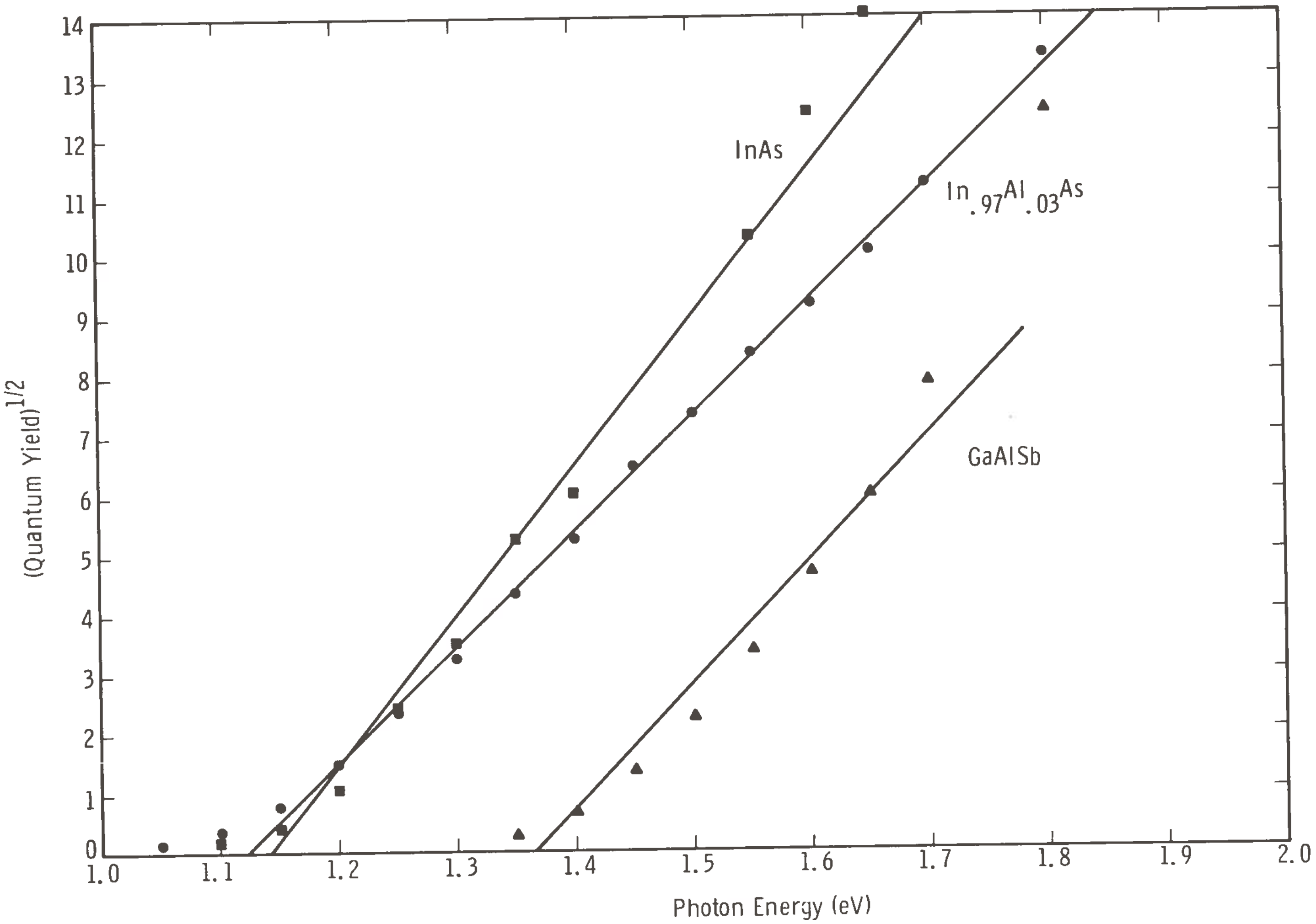

Figure 22. Thereshold Plots Comparing the Heterojunction Barrier Heights for Cs_2O Activated InAs, InAlAs, and GaAlSb

Even solving all the problems associated with Al would give us only two other possibilities, InGaAlAs and InAlAsP.

A preliminary investigation of the InGaAsP system has begun. An intelligent prediction of the liquid composition that will yield a particular solid solution on solidification is obtained from knowledge of the phase diagram for the quaternary system. Addition of a fourth component increases the complexity of both the equilibrium equations and the graphical representation. In the ternary system a three-dimensional plot with one of the axes as temperature can be used to represent solid and liquid composition at all temperatures. However, in a quaternary only the composition at a constant temperature can be depicted three-dimensionally. The liquidus surface and liquid-solid tie lines change producing a different figure at each temperature. A qualitative sketch for the InGaAsP system is shown in Fig. 23.

Connection between quaternary solid compositions and measurable physical quantities is achieved by a three-dimensional figure relating bandgap and lattice constant to composition. If Vegard's law is assumed as an extention from its proven validity for the ternaries, the unit cell size vs composition figure becomes a near planar lattice constant surface over a composition plane (lower half of Fig. 24). The bandgap surface is more irregular and may even have sharp edges (upper half of Fig. 24). These discontinuities result when the gap changes from direct to indirect with composition. If now a contour map is made of these surfaces by superposition over the composition plane, the drawing of Fig. 25 results. Composition is determined by measuring the bandgap and lattice constant, and locating where these quantities intersect. The bandgap values corresponding to a given composition were determined by interpolation from the ternary data. The "bowing parameter" (A in the equation $G = Ax^2 + Bx + C$) was varied linearly with composition in interpolating between the known values at the diagram edge.

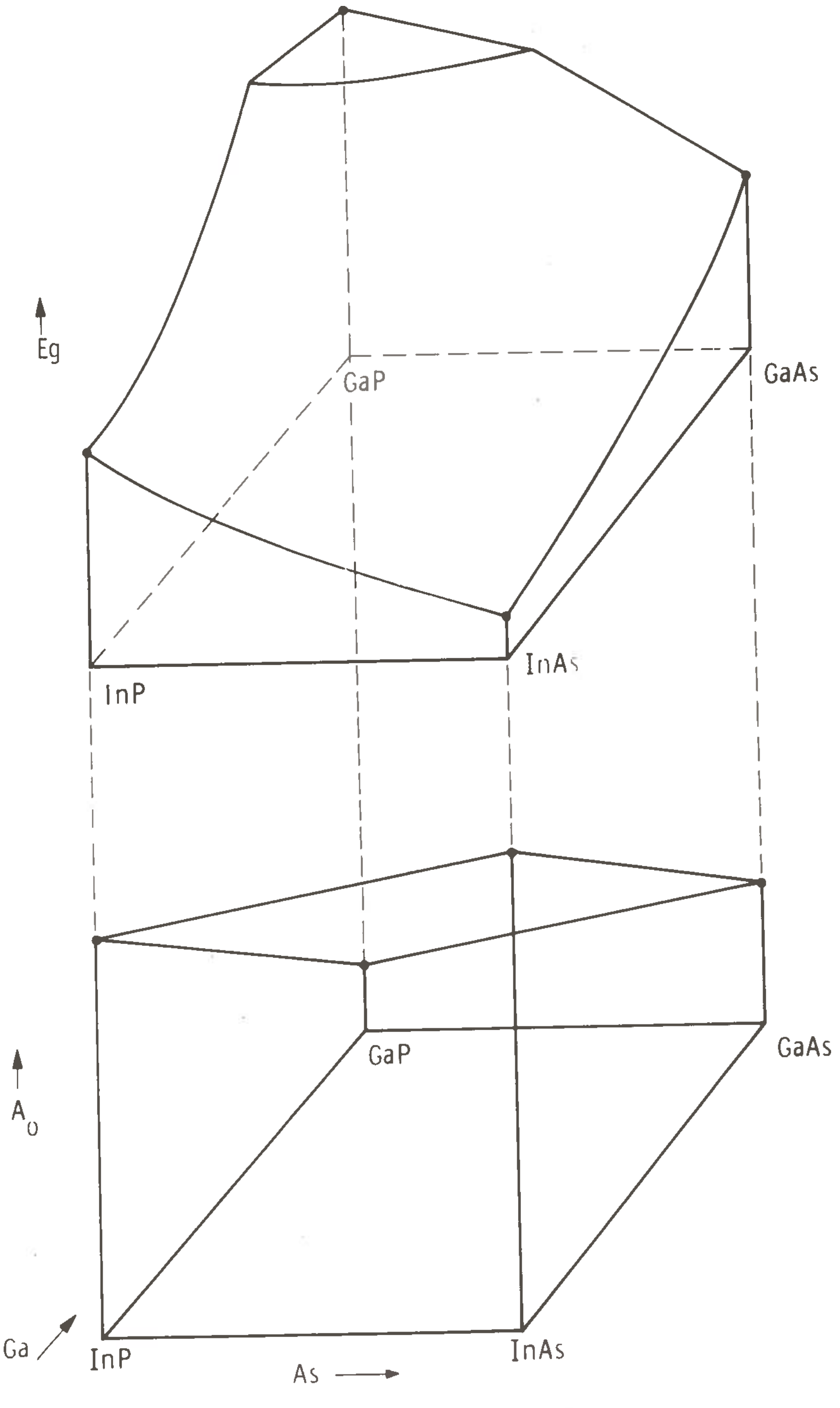

Figure 24. A qualitative drawing of the bandgap surface (upper figure), lattice constant surface (bottom figure) of the InGaAsP quaternary. The compositional plane is the base of both figures.

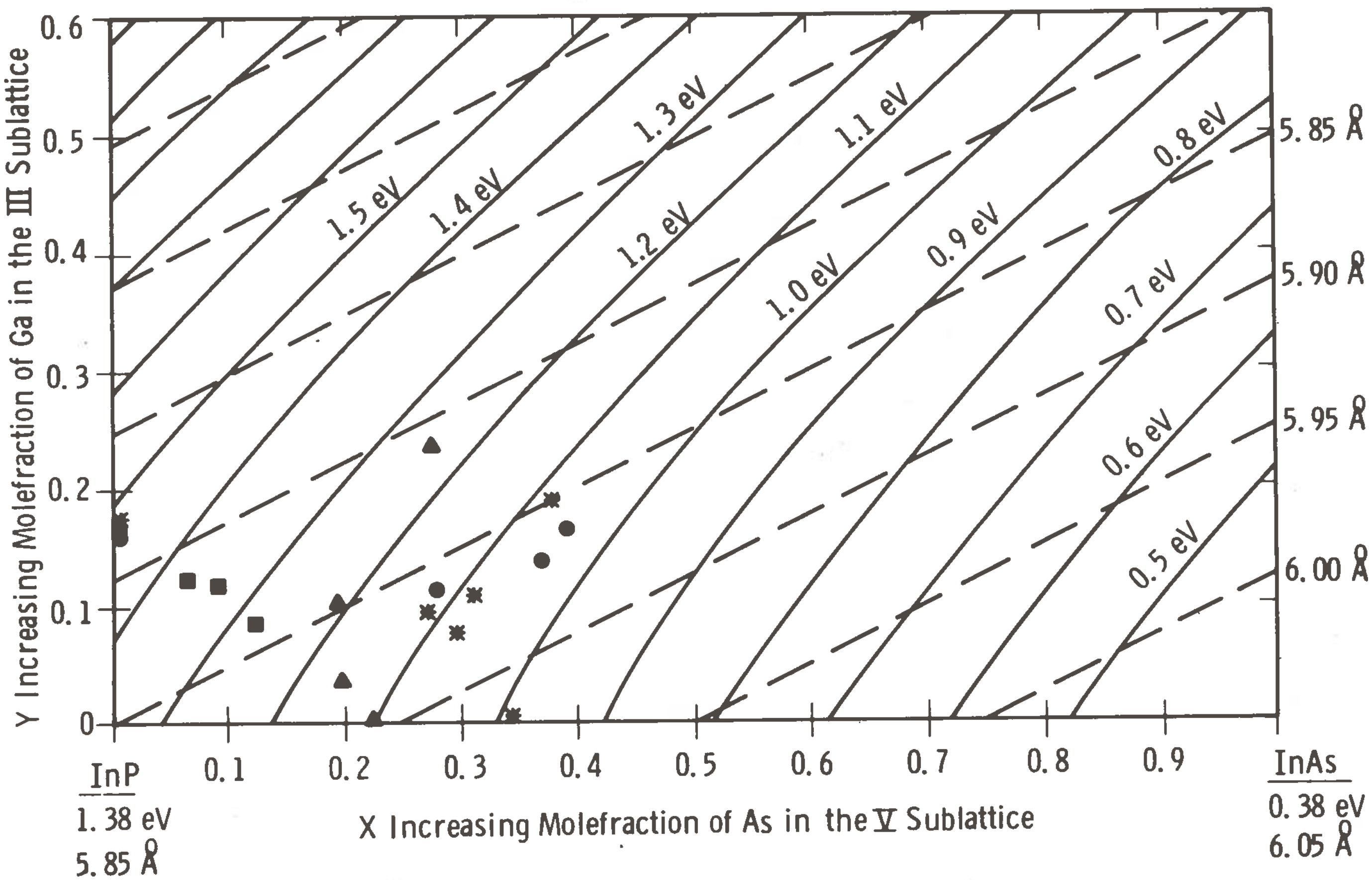

Figure 26. Bandgap-lattice-constant-composition plot for the LPE grown to date.

TABLE IV

GROWTH AND CHARACTERIZATION PARAMETERS FOR InGaAsP LAYERS

Sample	Weight(gm) In	Weight(gm) InAs	Weight(gm) Ga	α/o_{In}	α/o_{As}	α/o_{Ga}	Lattice Constant Substrate(Å)	Lattice Constant Epi Layer(Å)	Bandgap 77 °K (eV)
73	2.09285	.00797	.00400	.9946	2.288×10^{-3}	3.123×10^{-3}		5.7731	1.49
74A	2.09470	.00803	.00132	.9966	2.307 "	1.032 "	5.8588	5.8391	1.34
74B	"	"	.00307	.9953	2.304 "	2.396 "	5.8619	5.8199	1.405
74C	"	"	.00419	.9944	2.303 "	3.268 "	5.8588	5.8188	1.43
77A	2.09285	.04774	0	.9865	1.344×10^{-2}	0		5.8952	1.16
77B	"	"	.00210	.985	1.342 "	1.605×10^{-3}	5.8630	5.8786	1.21
79A	2.09	.0519	.00370	.9826	1.455 "	2.822 "	5.8619	5.8458	1.27
79B	2.09	"	.00567	.9811	1.453 "	4.318 "	5.8619	5.8110	1.30
81A	2.02415	.058	0	.9832	1.676 "	0	5.8630	5.9030	1.13
81B	"	"	.00238	.9814	1.673 "	1.867×10^{-3}	5.8630	5.8710	1.16
81C	"	"	.00412	.9800	1.671 "	3.229 "	5.8620	5.8370	1.26
81D	"	"	.00545	.9790	1.669 "	4.267 "	5.866	5.8260	1.27
85A	2.0605	.0745	0	.9790	2.097 "	0		5.9129	1.08
85B	"	"	.00247	.9772	2.093 "	1.887×10^{-3}	5.862	5.8708	1.11
85C	"	"	.00402	.9760	2.090 "	3.068 "	5.860	5.862	1.185
85D	"	"	.00634	.9743	2.086 "	4.831 "	5.862	5.831	
85E	"	"	.0085	.9727	2.083 "	6.466 "	5.858	5.8261	
92	2.05023	.08532	0	.9760	2.398 "	0	5.8609	5.9222	1.05
93	"	"	.00280	.9739	2.393 "	2.137×10^{-3}	5.8667	5.8843	1.15
94	"	"	.00468	.9725	2.389 "	3.566 "	5.8619	5.8697	1.17
95	"	"	.00644	.9712	2.386 "	4.900 "	5.8656	5.8510	1.145

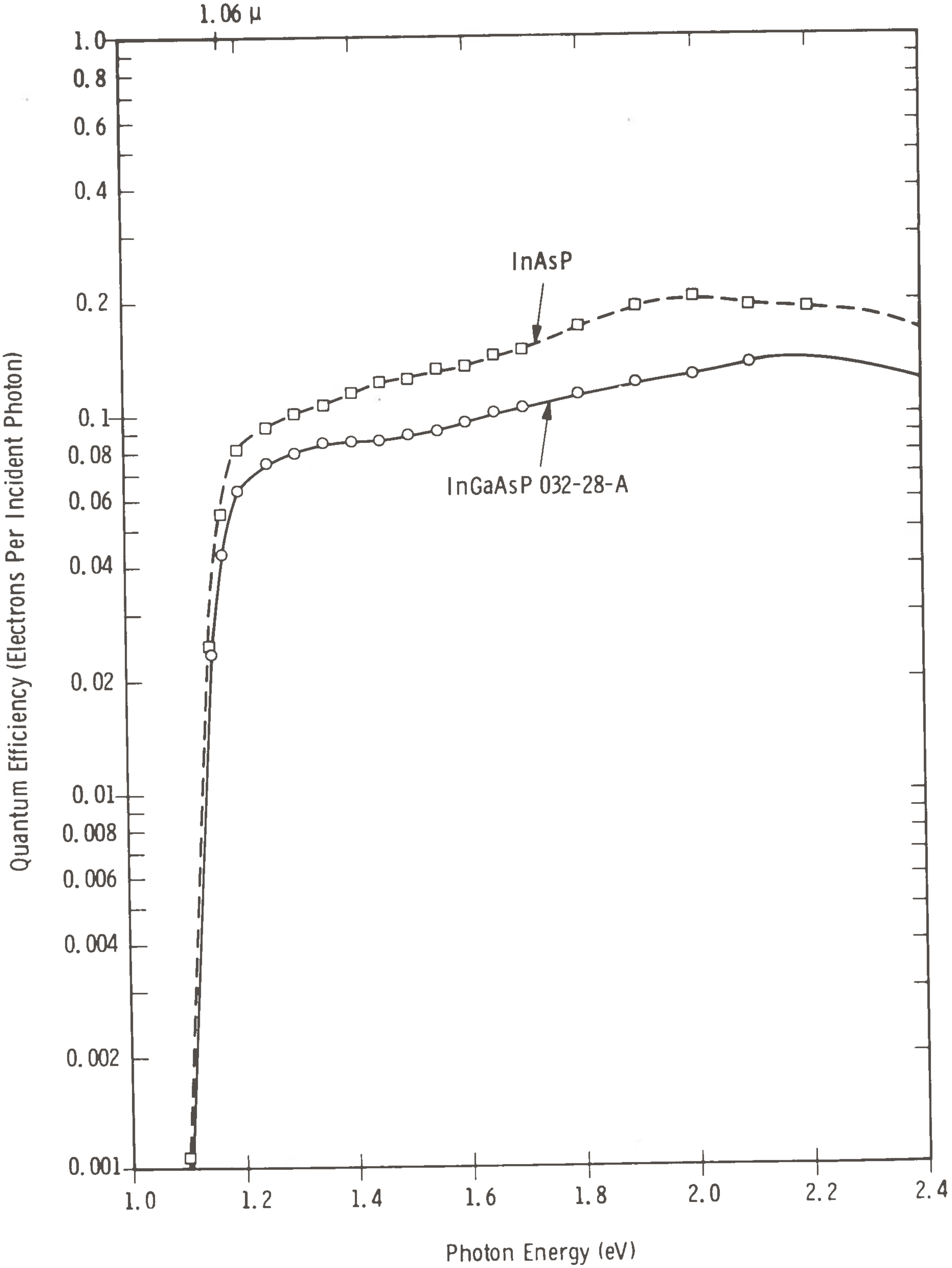

Fig. 28. Comparison of the yield curve of the InAsP photocathode giving the highest 1.06 μm quantum efficiency with that of the InGaAsP photocathode which was best at 1.06 μm.

TABLE V

HETEROJUNCTION BARRIER HEIGHTS ON P-TYPE GaSb

Activation Layer	Barrier Height
Cs_2O	1.23 ± 0.03 eV
CsSeTe	1.4 eV
K_2O	1.7 eV
CsRbS	1.35 eV
CsS	1.9 eV

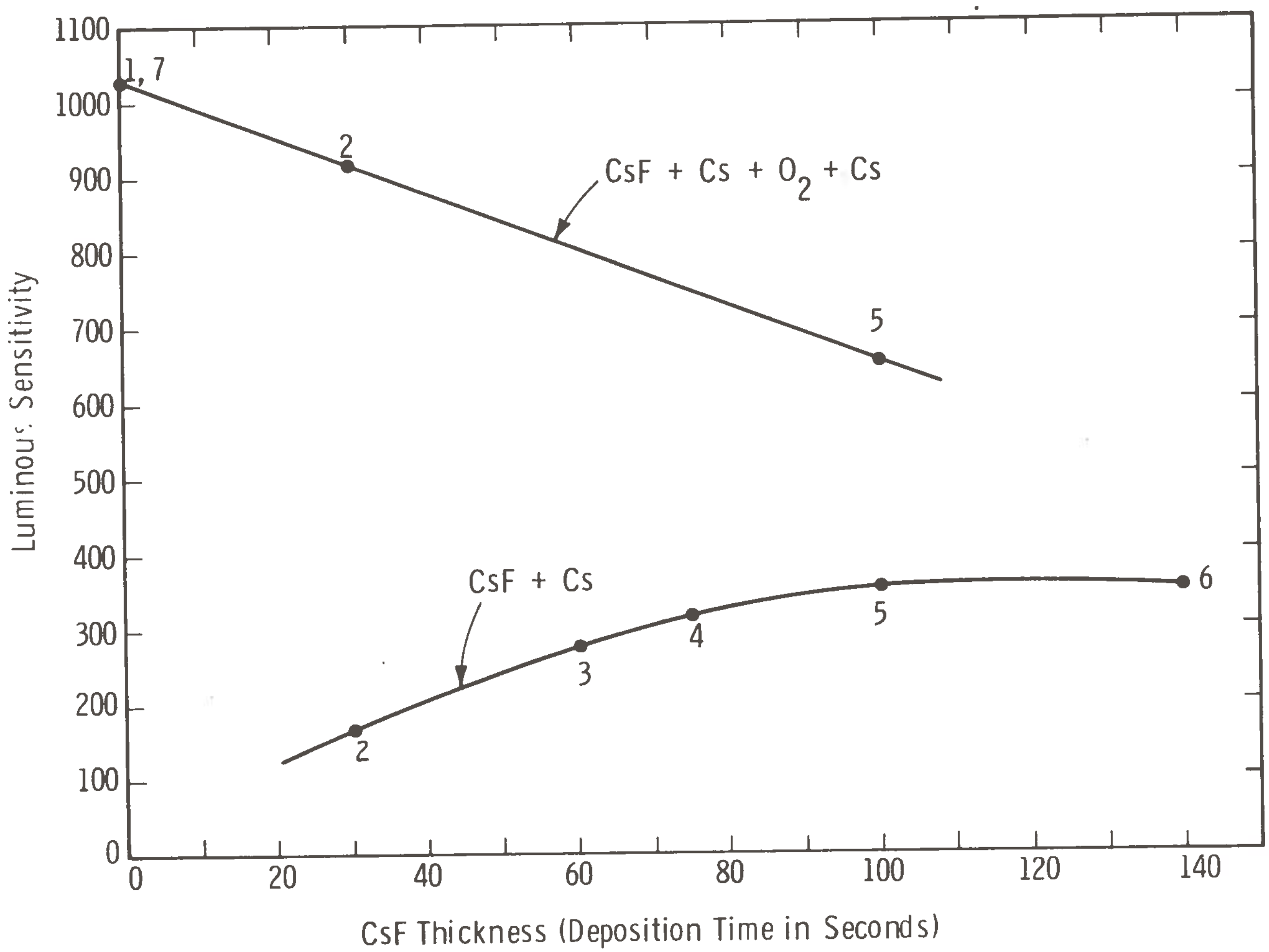

Figure 29. Comparison of CsF and Cs_2O Activation of a (111B) GaAs Sample. The yield after CsF + Cs exposure is shown as the lower line, and the yield after additional Cs and O_2 exposure, as the top line, versus the amount of CsF deposited on the sample.

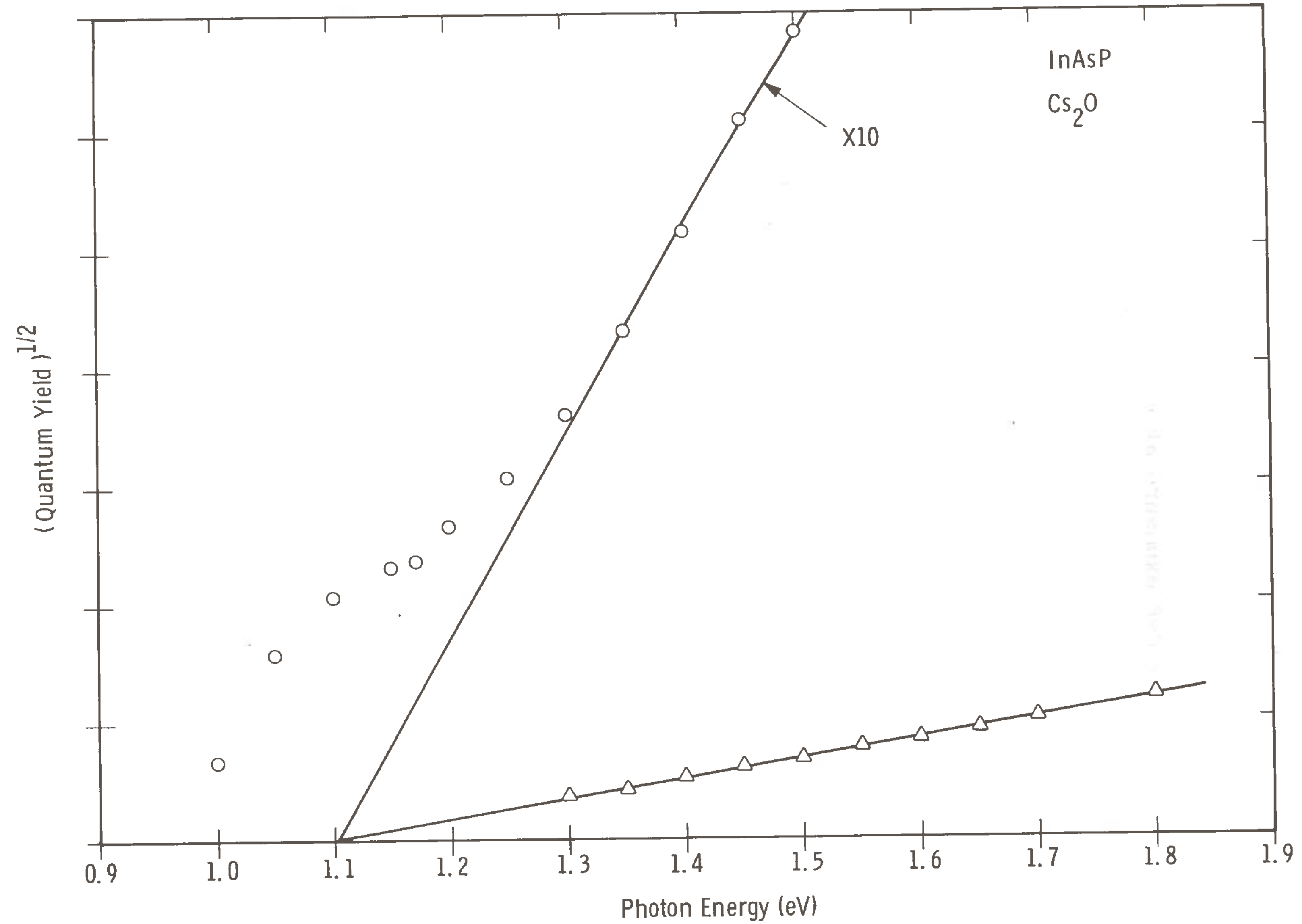

Figure 30. Threshold plot of the square root of the quantum efficiency vs photon energy demonstrating a 1.10 eV heterojunction barrier with Cs_2O activation of a 1 eV bandgap p-type InAsP sample.

E. Use of Different Surface Preparation Methods

The position of the bands at the heterojunction interface is determined by the surface states. These states are in turn determined by the type of surface atom and by the position and type of its surroundings. The section on orientation dependence showed the clear effect of change in surface atom type (from In or Ga to As or P) in going from {111A} to {111B} orientation. The change in InAsP band bending and barrier height with As concentration on the {111B} face again pointed this out. The change with faceting of the {111A} face of GaAs showed clearly how treatment of a surface could change the surface atom positions and hence the surface states. For the case of {100} Si, the special surface arrangement (as seen by LEED) required to set up the desirable surface dipole arrangement again indicates the importance of surface treatment. Some treatments may change the ratio of surface atoms in an edge position to surface atoms in a plane position. Some treatments may not change the basic surface structure, but may anneal out damage and defects in the near-surface region which will become the band-bending region in the actual device. What ever surface treatment is used, its prime function must be to leave the surface in a clean, undamaged state.

Our normal activation procedure is to take an as-grown or chemically-polished surface from the liquid epitaxial furnace through a vacuum interlock into the ultrahigh vacuum chamber where it is heated to near the congruent evaporation point for a few minutes. It is then cooled to room temperature where it is activated with Cs and O. An additional step has been added to this procedure which results in higher quantum efficiencies from InGaAs. After the initial activation of the photocathode, it is reheated to about 100°C below the congruent evaporation point for several minutes. It is then cooled to room temperature and reactivated. Figure 33 shows two yield curves taken on a 1.25 eV bandgap (too high for good 1.06-micron yield) InGaAs sample, before and after this extra heat treatment. About a 10% improvement in quantum yield is seen consistently on InGaAs samples by using this treatment. Some part of the initial Cs_2O layer remains after the lower temperature heat treatment. The same treatment is not effective for InAsP samples. No measurements have been made on n-type samples to see if this procedure affects the heterojunction parameters as the InGaAs diffusion length remains a problem limiting its use.

A possible cause of less than ideal performance of ternary III-V photocathodes is traps caused by defects in the band-bending region or micro-inhomogeneities. To test for this possibility, a 1.20 eV bandgap InGaAs sample was activated as normal, and its quantum yield curve was measured. This curve is the bottom curve in Fig. 34a. It was then re-heated to just below the congruent evaporation point for a few minutes to remove all the Cs_2O. It was then cooled by 70°C and allowed to anneal at that temperature in the ultrahigh vacuum chamber for 16 hours. It was then reheated to the initial heat-cleaning temperature, cooled, and activated. As can be seen by the top curve of Fig. 34a, the yield nearly doubled.

InAsP cathodes are quite sensitive to the actual heat-cleaning temperature. The best results have been obtained from cathodes which are heated just to the point where the decomposition process starts. Both InAsP and InGaAsP retain their {111B} surface orientation after heating in contrast to GaAs which facets to {110} surfaces from an original {111B} face. Figure 34b shows the hexagonal LEED pattern characteristic of a {111} face from a properly heat-cleaned InGaAsP sample.

During the course of this contract, refinements in our surface preparation and heating techniques have led to about a 40% improvement in escape probability for 1.06-micron InAsP samples resulting from a lowering of the heterojunction barrier to 1.1 eV

<u>Figure 34b</u>. Hexagonal LEED pattern from a properly heat-cleaned {111B}-oriented InGaAsP sample.

changes is a significant increase in diffusion length, and hence in 1.06-micron quantum efficiency during the course of this contract. Figure 35 shows the improvement obtained. The lowest curve represented the state-of-the-art at the beginning of this contract. The upper curves are for three cathodes activated after the material quality was improved. #111-4-A and #111-10-C were in photodiode tubes and #111-8-A was in a high vacuum chamber. The higher yields at 1.06 microns were obtained mainly by improved InAsP material quality with some improvement in activation techniques. The improvement in escape probability through improvements in activation techniques with time may be gauged by comparing the 1.65 eV quantum efficiency which is up about 40% from ID #14 to #111-10-C. The remaining 90% improvement in 1.06-micron quantum efficiency may be accounted for by an increased diffusion length. This is clearly seen on the yield curves of Fig. 35 by the flatter response curve and sharper corner at threshold for the more recent material.

A further increase in 1.06-micron yield would result from any increase in the optical absorption coefficient at 1.06 microns which resulted in eventual promotion of electrons into the conduction band and which did not change the other cathode parameters. Such an increase in optical absorption coefficient can be obtained by amphoteric doping, that is, by doping simultaneously with p-type and n-type dopants. The dopants will have energy levels several millivolts into the forbidden energy gap from the edges of the conduction and valence band. Optical transitions can take place from both the acceptor level and the valence band to both the donor level and the conduction band. Excitons bound to a donor-acceptor pair can also be created. These additional processes add to the optical absorption coefficient. Excitons can be thermally broken up into holes and free electrons, and electrons in donor levels can be thermally excited to the conduction band, giving free electrons which can then contribute to photoemission.

Both Si and Ge are known to be amphoteric dopants in liquid epitaxial GaAs. The amount of compensation and the total impurity concentration may be varied by varying the growth temperature and the Si or Ge concentration in the melt. Figure 36 shows a comparison of photoemission measurements on a Zn-doped GaAs sample compared with a Si-doped sample (Ref. 35) and with a Ge-doped sample (Ref. 36). The solid curves are the actual measured photoemission data. The dotted curves for the Si and Ge-doped samples are normalized to the Zn-doped sample's curve at 2.0 eV to show the comparison as if all three samples had nearly the same escape probability. It is not clear whether the lower escape probability observed on the Si-doped and Ge-doped samples is due to the use of those dopants, or to poorer cleaning and activation techniques used by the other experimenters. At least in the case of the Si-doped sample, the second explanation seems likely, as Garbe and Frank report on a Zn-doped sample in the same publication which appears to have an escape probability identical to that of one of their Si-doped samples.

As can be clearly seen from the normalized curves, there is a significant increase in the number of photoexcited electrons in the region of 1.395 eV, 30 meV below the bandgap, in both the Si and Ge-doped samples. As the optimized 1.06-micron InAsP photocathode has a bandgap of 1.2 eV, 30 meV above the desired photon energy, we might expect about a 50% improvement in 1.06-micron quantum efficiency if the amphoteric doping technology could be transferred to InAsP with no loss in material quality or in escape probability.

Experiments were done with liquid epitaxial growth of InAsP from melts containing either Si or Ge. In all cases, the samples were n-type, with the additional complication that Si could not be incorporated into the solid in very large concentrations such as are required for photoemitters. Thus in order to obtain a compensated p-type InAsP sample, it appears to be necessary to use a p-type dopant such as Zn in addition to Si or Ge. A sample (#91-13-A) was grown from a melt containing Zn such as to give a Zn acceptor concentration of $10^{19}/cm^3$. It was activated, and the measured quantum yield curve is shown in Fig. 37. Sufficient Ge was then added to the melt to give a Ge donor concentration of $10^{18}/cm^3$. The quantum yield curve from the sample grown from this melt (#91-15-A) is also shown in Fig. 37. Apparently the addition of the Ge caused a large decrease in diffusion length (from 3 to 0.5 micron) which more than cancels the increase in near-bandgap optical absorption.

Another possibility besides doping with Zn and a donor is to dope with Zn and the isoelectronic dopant N. Nitrogen has the advantage that it introduces a spatially localized energy level just below the conduction band, similar to a donor level, and yet it introduces no compensation of the p-type dopant (Zn) since it is itself a column V element which goes on a column V site.

Figure 38 shows the photoemission results from three InAsP samples which were grown by liquid epitaxy from a standard melt with NH_3 added to the H_2 gas flow through the furnace. The actual N concentrations have not been measured, but were estimated from results of N doping of liquid epitaxial GaP. A fourth sample with an even higher nitrogen concentration gave poorer results. For some unknown reason, the escape probability of all of these samples, including the control sample which was grown first with no nitrogen from the same melt, was lower than optimum. The yield curve of the control sample was nearly identical to that of the "1×10^{17}" sample. It appears that the predicted 50% increase in αL at 1.06 microns has been achieved; however, it remains to be conclusively demonstrated that the N doping was in fact responsible and that high escape probabilities can be obtained from N-doped samples.

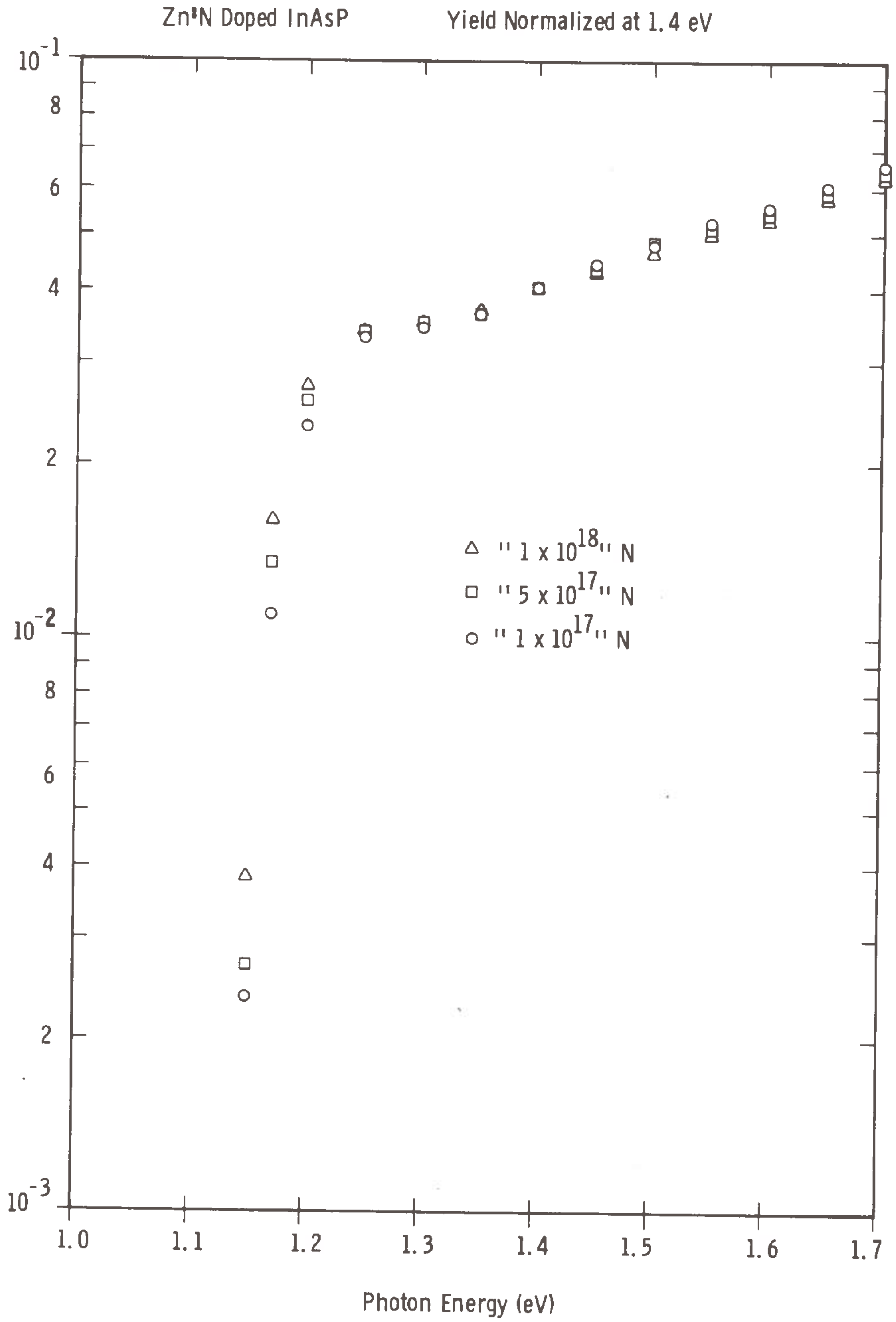

Figure 38. Normalized quantum yield curves of three InAsP samples grown from the same melt with increasing N doping concentration. The N doping levels are estimated.

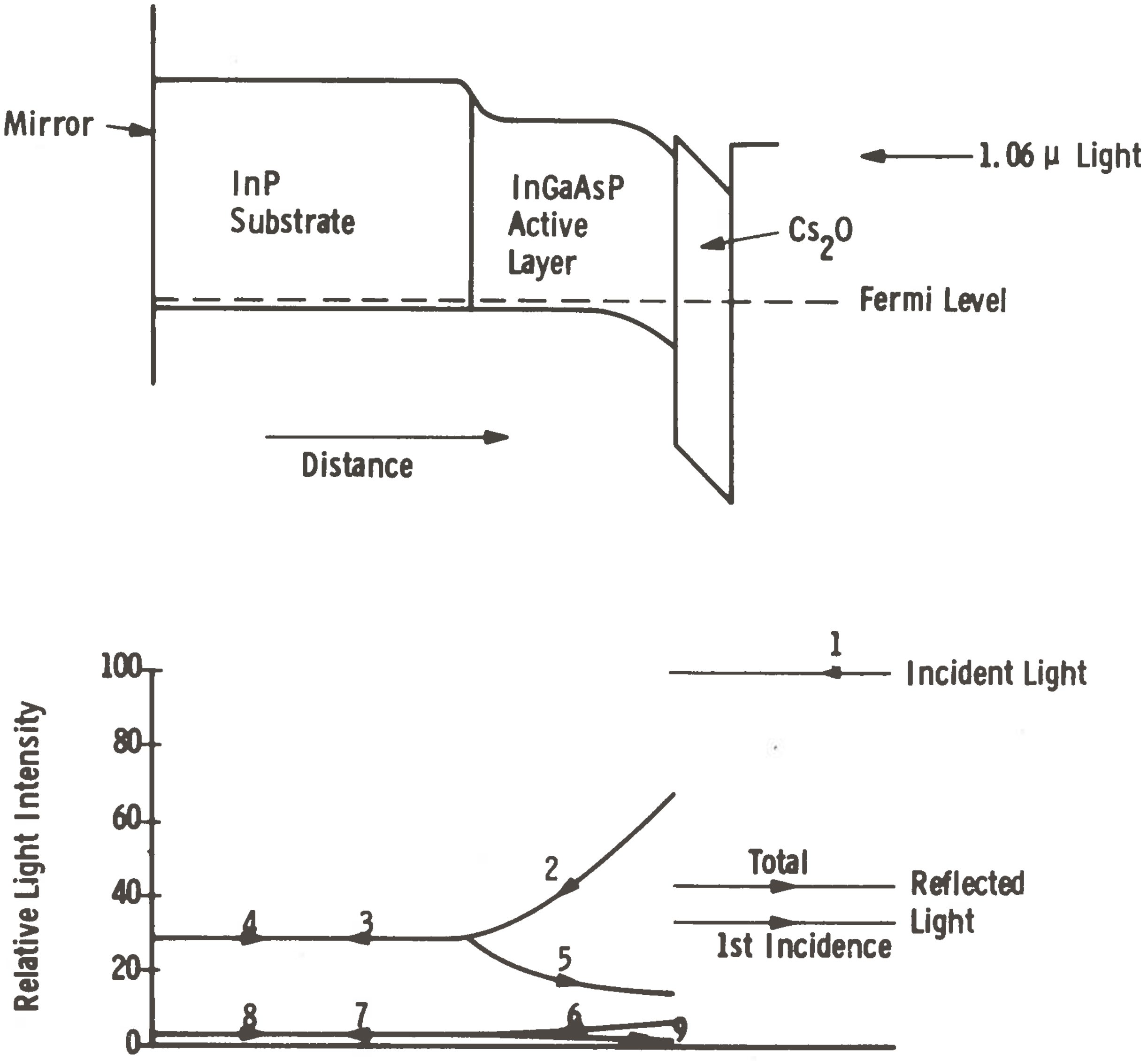

Figure 39. The top figure shows the band diagram for a heterojunction mirror structure photocathode. The horizontal scale represents distance perpendicular to the emitting surface, but is not drawn to scale. The bottom graph has the same distance calibration on the horizontal axis and shows on the vertical axis the relative intensity of the 1.06-micron light on its multiple passes through the photocathode, with the numbered arrows tracing the path.

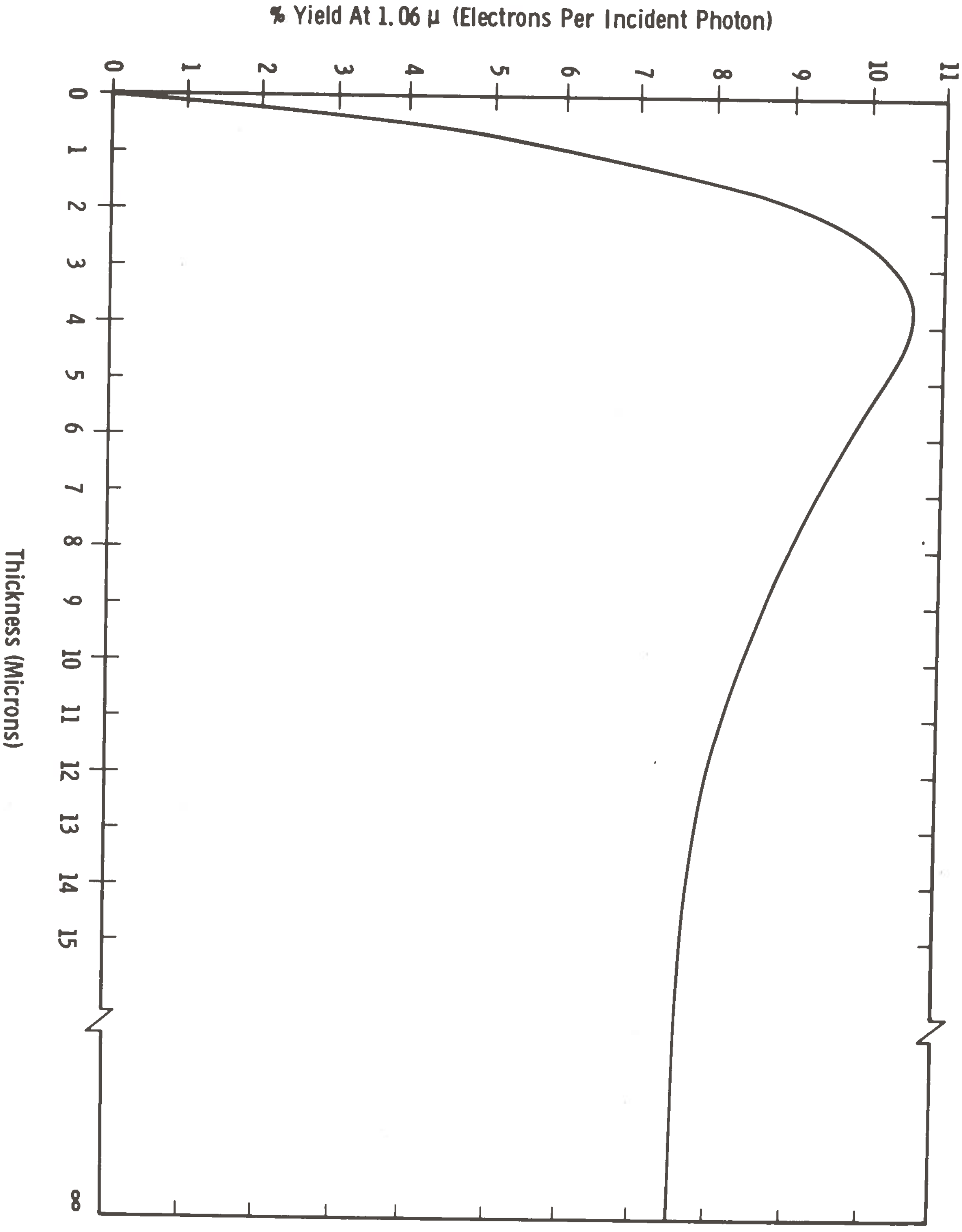

Fig. 40. Predicted quantum yield at 1.06 μm vs active layer thickness for the cathode shown in Fig. 39. The parameters used for the calculation are hν = 1.17 eV, L = 5 μm, bandgap = 1.19 eV, interfacial recombination velocity = 0.

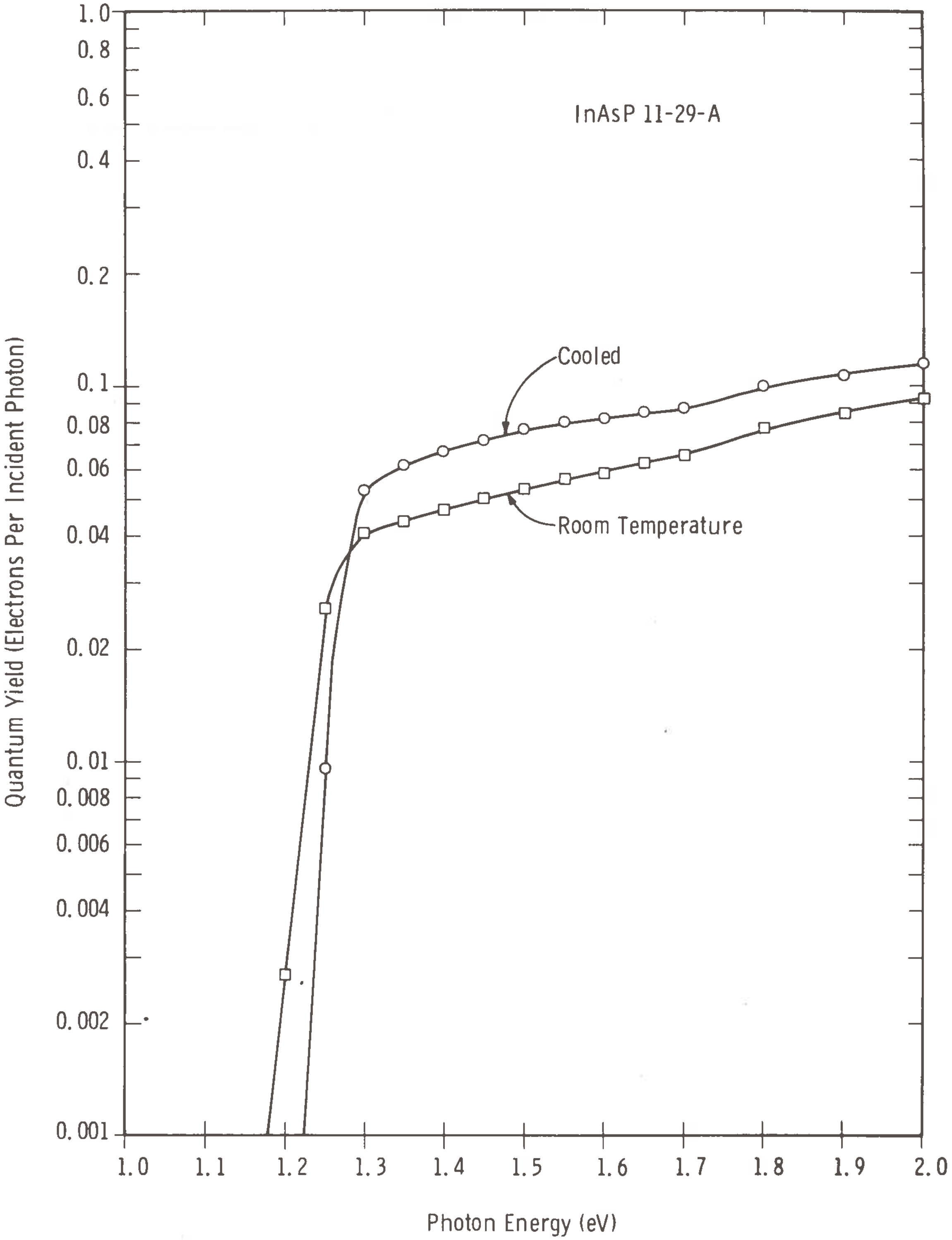

Fig. 41. Comparison of room temperature and cooled yield curves showing the effects of cooling on an InAsP photocathode.

too low for optimum 1.06-micron yield. Upon cooling, the 1.06-micron quantum efficiency increased to 7.5%. This was the highest 1.06-micron quantum efficiency yet measured. The bandgap was probably a little high for optimized cooled operation, so further improvements can be expected with further work.

CONTAMINATION SOURCES

Contamination of the photocathode surface must be prevented in order to ensure the highest possible quantum yield. Auger spectroscopy has proven to be a valuable tool in discovering and eliminating contamination sources.

Carbon is the most difficult contaminant to get rid of, and it is one which does have a known bad effect on photocathode escape probability. Some carbon contamination remains even after considerable effort to eliminate it. The Auger spectrum of a typical InAsP sample is shown in Fig. 44 with the principal Auger peaks identified. The carbon on this sample is roughly 5% of a monolayer.

A source of contamination which has been identified with Auger spectroscopy during the period of this contract is shown in Fig. 45. Samples always showed a reduced escape probability after sitting overnight in electronic grade methanol before being transferred into the high vacuum chamber. The Auger spectrum shows that a significant amount of copper was deposited on the InAsP surface even though the Cu concentration in the methanol was analyzed to be 1 part in 10^7. Sulfur and carbon were also deposited on the surface. The surface Cu would diffuse into the sample during heat-cleaning, producing harmful electron traps.

Continuous attention to all possible contamination sources is necessary if the highest quantum yields are to be obtained.

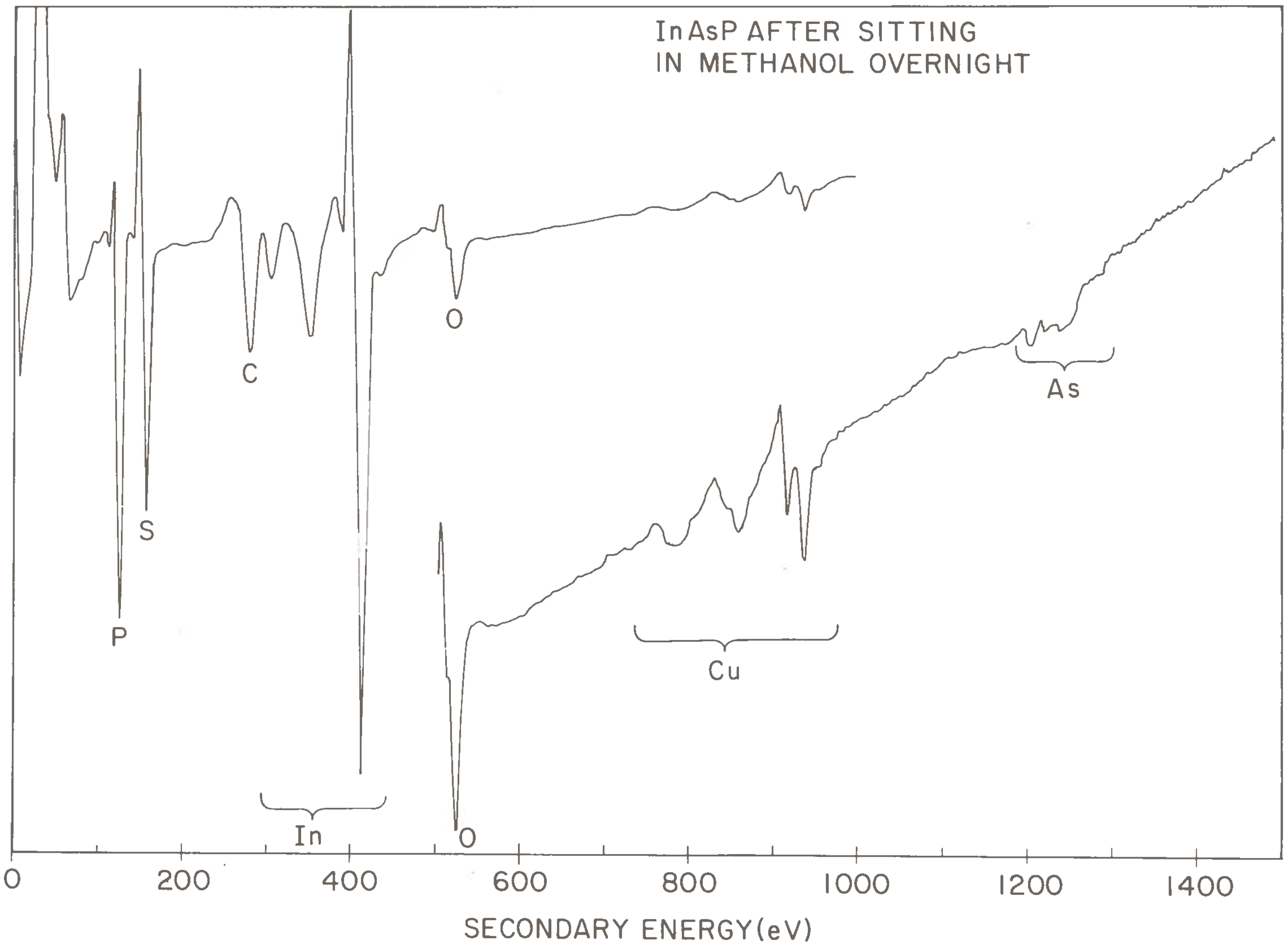

Figure 45. Auger spectrum of an InAsP sample which was contaminated by sitting in methanol overnight.

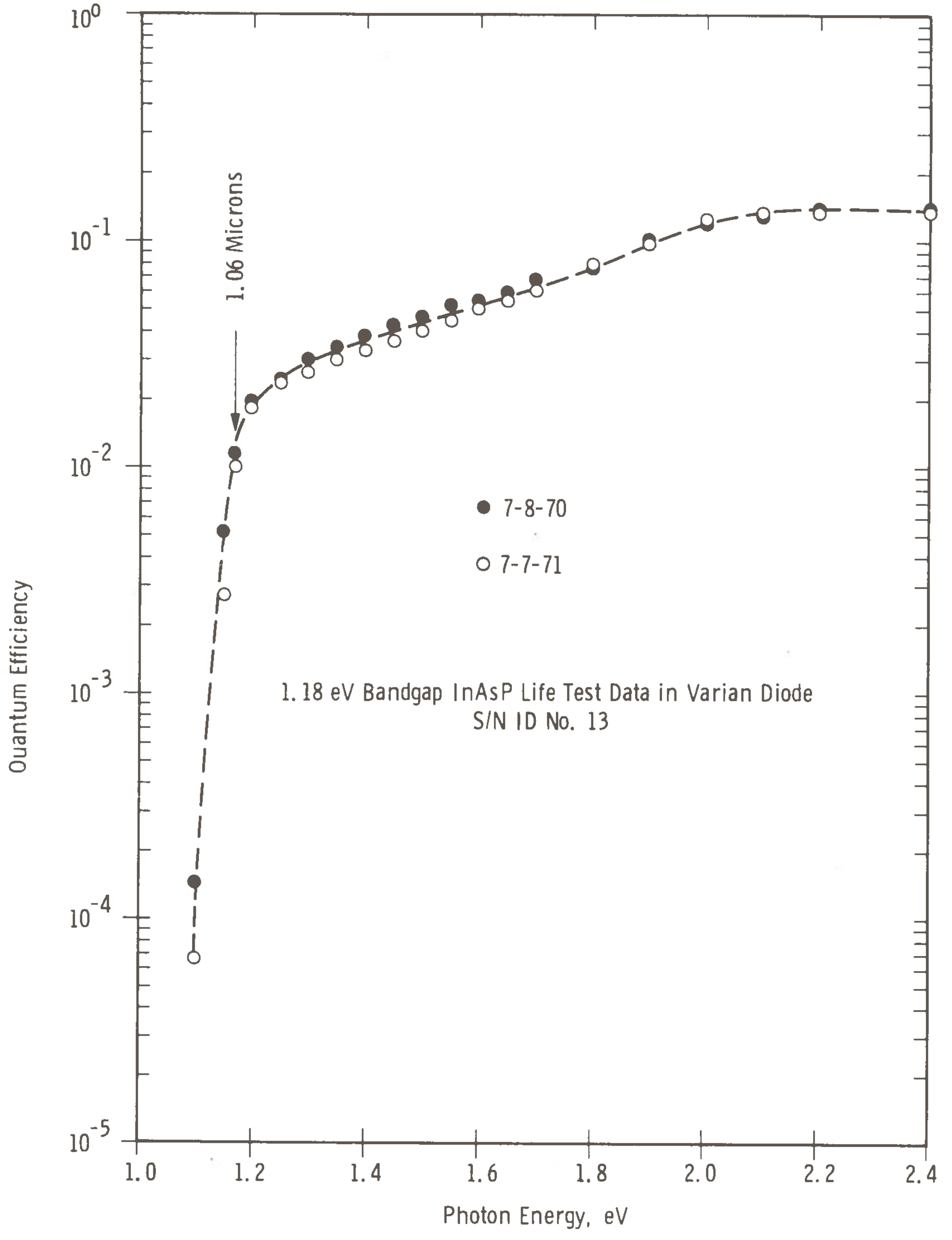

Figure 46. Two quantum yield curves taken just after pinch-off and one year later on an InAsP photocathode in a photodiode, demonstrating stability of performance.

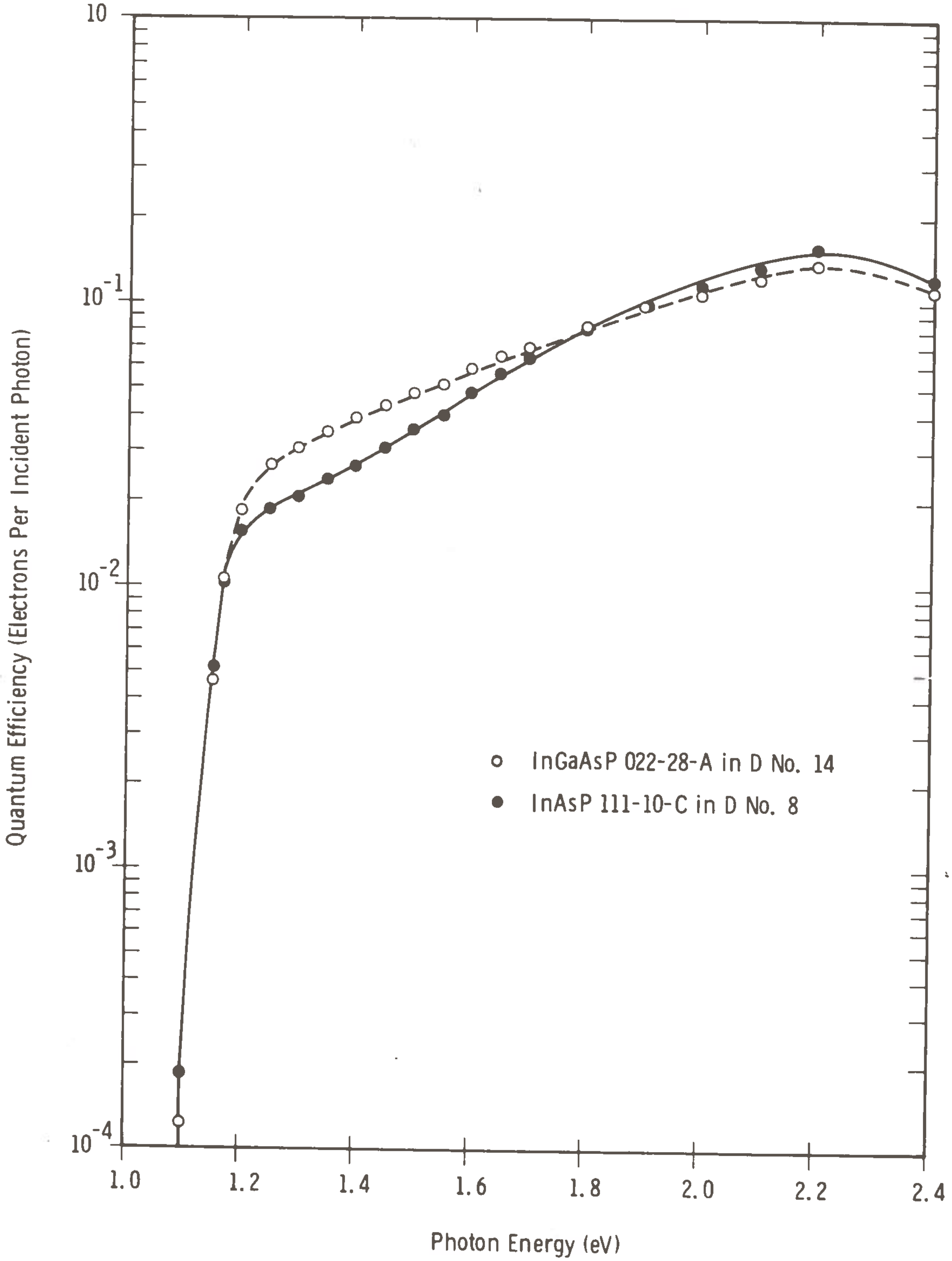

Figure 48. Quantum yield curves of the photocathodes in the two diodes which were shipped on this contract at the time of shipment.

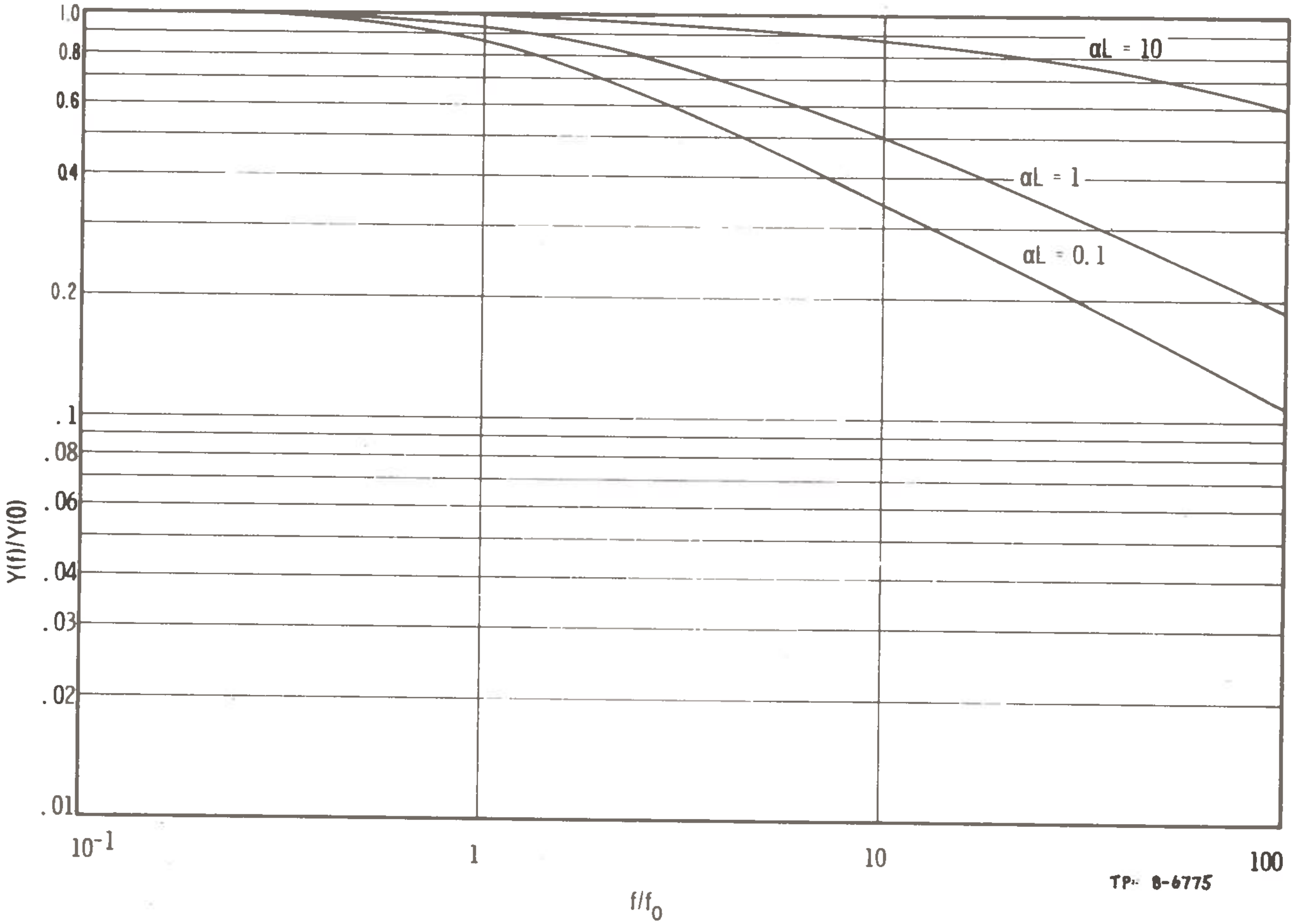

Figure 49. Normalized Frequency Response of III-V Photoemitters Used as Amplitude Modulation Detectors.

CONCLUSIONS

The work reported has shown that a program of empirical development of negative-affinity photocathodes for 1.06 microns, guided by general theoretical understanding of the limitations imposed by the 3-5 activator layer heterojunction, can lead to significant advances in performance. The highest quantum efficiency experimentally obtained during the course of this program was 7.5% (electrons per incident photon), observed from a cooled InGaAsP quaternary {111B}-face sample activated with (Cs,O). A quantum efficiency of over 10% is predicted for this system in a mirror structure photocathode. Many other materials, different crystal faces, and activator layers were investigated in arriving at this result.

The heterojunction barrier model was substantiated and repeatedly confirmed in the course of these investigations. Of the 3-5/activator systems, the above produces the lowest barrier height, the highest escape probability, and the longest minority carrier diffusion length.

Gradual improvement in materials and tube technology have generated improved stability of these cathodes in the high performance ranges. Further study of the contamination problems giving rise to the remanent slow instabilities of the high performance cathodes is indicated.

REFERENCES (Contd.)

19. G. B. Stringfellow and P. E. Greene, J. Phys. Chem. Solids 30, 1779 (1969).

20. M. Ilegems and G. L. Pearson in Proc. 1968 Symposium on GaAs (Conf. Series #7, IPPS, London, 1969), p. 3.

21. G. A. Antypas and L. W. James, J. Appl. Phys. 41, 2165 (1970).

22. M. B. Panish and M. Ilegems in Proc. 1970 Symp. on GaAs and Related Compounds (Conf. Series #9, IPPS, London, 1971), p. 67.

23. I. Prigogine and R. Defay, Chemical Thermodynamics (John Wiley, New York, 1962).

24. L. J. Vieland, Acta Met. 11, 137 (1963).

25. C. D. Thurmond, J. Phys. Chem. Solids 26, 785 (1965).

26. B. D. Lichter and P. Sommelet, Trans. Met. Soc. AIME 245, 99 (1969).

27. M. Ilegems, Tech. Report #5119-1, SU-SEL-69-054, Stanford Electronics Lab, Stanford University, October 1969.

28. G. A. Antypas, private communication.

29. I. I. Burdiyan and A. S. Borshchevskii, Soviet Phys. - Tech. Phys. 3, 28 (1968).

30. B. Predel and H. Sandig, Matl. Sci. Eng. 4, 49 (1969).

31. L. M. Foster and J. E. Scardefield, J. Electrochem. Soc. 118, 495 (1971).

32. B. D. Lichter and P. Sommelet, Trans. Met. Soc. AIME 245, 1021 (1969).

33. S. Garbe, Phys. Stat. Sol.(a) 2, 497 (1970).

34. T. Thalhammer, PSEE Conference, U. Minnesota, August 1971.

35. S. Garbe and G. Frank in Proc. 1970 Symp. on GaAs and Related Compounds (Conf. Series #9, IPPS, London, 1971), p. 208.

36. H. Schade, H. Nelson, and H. Dressel, Appl. Phys. Letters 18, 121 (1971).